

國立台灣大學理學院天文物理研究所
碩士論文



Institute of Astrophysics
College of Science
National Taiwan University
Master Thesis

於國聖核電廠之高純鍍探測器背景的理解與研究
Background Studies and Understanding for High-Purity
Germanium Detector at Kuo-Sheng Neutrino Laboratory

陳璟翰

Jing-Han Chen

指導教授：王名儒 博士

共同指導：王子敬 博士

Advisor: Min-Zu Wang, Ph.D.

Co-Advisor: Henry Tsz-King Wong, Ph.D.

中華民國 105 年 8 月

August, 2016

國立臺灣大學碩士學位論文
口試委員會審定書

於國聖核電廠之高純鍍探測器背景的理解與研究
Background Studies and Understanding for High-Purity
Germanium Detector at Kuo-Sheng Neutrino Laboratory

本論文係陳璟翰君R02244010在國立臺灣大學物理學系、所完成之碩士學位論文，於民國105年07月21日承下列考試委員審查通過及口試及格，特此證明

口試委員：

王名儒

(簽名)

(指導教授)

王子敬

劉永邦



Abstract

To observe the neutrino-nucleus coherent scattering and dark matter searching, a detection system with ultra-low energy high purity germanium detector has been built up by TEXONO Collaboration in Kuo-Sheng Nuclear Power Plant. Due to the rarity and small recoil energy of these processes, understanding the background sources and their contribution to the energy spectrum are the key factors in this experiment. By using a data analysis toolkit called ROOT which was developed by CERN to reproduce the background, comparing to the experimental data, we can estimate the upper limit of 3H beta decay activities in HPGe crystal. In data analysis, the p-type Germanium detector has a surface effect which will distort the energy deposit in the surface of Ge crystal, a charge collection efficiency function is to determine the energy loss because of the surface effect. By ROOT and a simulation toolkit GEANT4, we can try to find out the possible structure of charge collection efficiency in Ge surface.

摘要



爲了觀察微中子-原子核的相干散射與尋找暗物質，台灣微中子研究團隊於國聖核能發電廠建造了一個使用極低能高純鍺探測器的探測系統。因爲這些稀有的物理過程與微小的反衝能量，在這個實驗中了解背景的組成與他們在能譜中的貢獻是關鍵因素。使用CERN開發的資料分析工具ROOT來重現背景並與實驗數據做比較，我們可以估算出氙在高純鍺晶體中 β 衰變量的上限。在數據分析時，p型的鍺探測器會有表面效應造成存放於鍺晶體表面的能量失真，電荷收集效率函數可以決定因爲表面效應所造成多少的能量損失。使用ROOT與模擬工具GEANT4，我們可以試著找出電荷收集效率函數在鍺晶體表面可能的結構。



Contents

Abstract	i
List of Figures	vi
List of Tables	xii
Chapter 1 Overview	1
1.1 TEXONO Overview	1
1.2 A Brief Introduction to Neutrino	2
1.3 A Brief Introduction to WIMPs	3
1.4 The Goal of TEXONO	3
1.4.1 Neutrino-Nucleus Coherent Scattering	3
1.4.2 Dark Matter Searching	5
Chapter 2 Experimental Setup	6
2.1 Kuo-Sheng Neutrino Laboratory	6
2.2 Shielding	7



2.2.1	Passive Shielding	8
2.2.2	Active Shielding	10
Chapter 3 The Surface Effect of p-type Germanium Detector		16
3.1	p-type Point Contact Germanium Detector	16
3.1.1	Germanium Detector Configuration	16
3.1.2	Surface Layer	18
3.2	Charge Collection Efficiency in Transition Layer	24
3.2.1	Simulation and Measurement Data Taking Environment	24
3.2.2	T-function Profile	27
3.2.3	Hyperbolic Tangent Profile	32
Chapter 4 Data Analysis		36
4.1	Parameterization	36
4.2	Event Selection	38
4.2.1	Basic Cuts	38
4.2.2	Cosmic Ray Veto	41
4.2.3	Anti-Compton Veto	43
Chapter 5 Internal Background		47
5.1	Introduction	47
5.2	Background Sources	48
5.2.1	Neutron Background	48



5.2.2 Photon Background	49
5.3 X-ray peaks	51
5.4 Tritium Upper Limit	54
5.5 Summary	57
Chapter 6 Summary	59
Bibliography	61

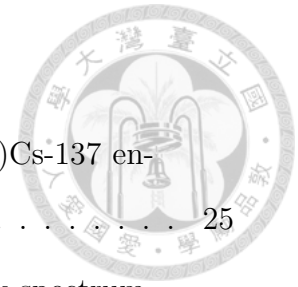


List of Figures

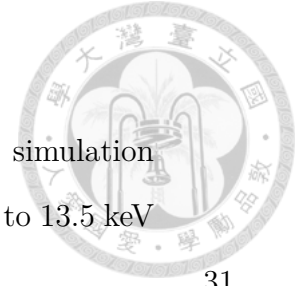
1.1	Expected integral $\bar{\nu}_e$ -N coherent scattering rates due to Standard Model contributions at the flux $\phi(\bar{\nu}_e) = 10^{13} \text{ cm}^{-2} \text{ s}^{-1}$, where “ee” denote electron-equivalent energy, assuming realistic detector resolution.	4
1.2	Recoil spectra for χ -Ge interactions at a crosssection of 10^{-40} cm^2 with different values of m_χ . Assuming an 1 kg-year data and background level at $1 \text{ kg}^{-1} \text{ keV}_{ee}^{-1} \text{ day}^{-1}$	5
2.1	Schematic side view of the Kuo-Sheng nuclear reactor building, and relative location of the reactor core and KSNL site (not drawn to scale).	7
2.2	The shielding design for KSNL, including the shielding material and the dimension of each layer.	9
2.3	Schematic layout of the 16 cosmic ray veto plastic scintillators.	11
2.4	Photograph of the plastic scintillators (the black panels) at the front side and their attached PMTs on upper ends.	12
2.5	Schematic side view of the set up inside the passive shielding.	14



3.1	(a) P-type semi-coaxial germanium detector, the p contact in this configuration is cylindrical. (b) P-type point contact germanium detector, the capacitance is lower in this configuration because the p contact shrink to a tiny disk (about 5 mm in diameter).	17
3.2	(a) N-type PCGe which have a thin, ion-implanted p^+ outer contact. (b) P-type PCGe which have a thick, lithium n^+ outer contact. . . .	18
3.3	(a) Hyperbolic Tangent. The structure of the charge collection efficiency in an 1 mm surface layer with using hyperbolic tangent.	20
3.4	(b) Sigmoid Function. The structure of the charge collection efficiency in an 1 mm surface layer with using sigmoid function.	21
3.5	(c) T-function. The structure of the charge collection efficiency in an 1 mm surface layer with using T-function.	21
3.6	The pulse for bulk(left side) and surface(right side) near threshold, the rise time of the surface pulse is longer.	22
3.7	In log rise time vs. energy plot, we can clearly see that for energy greater than 2 keV, it is easy for us to distinguish surface and bulk events because the events are divided, but the events below 2 keV are mixed and difficult for us to distinguish.	23
3.8	(a) The geometry of 900g p-PCGe detector in GEANT4. (b) Events starting points are distributed on a disk at the top of the detector, and traveling n -z direction.	25



3.9	(a) Am-241 energy spectrum simulated by GEANT4. (b)Cs-137 energy spectrum simulated by GEANT4.	25
3.10	The measurement of Am-241 high energy and low energy spectrum. Most of the events are stopped and deposit their energy in the surface.	26
3.11	The measurement of Cs-137 high energy and low energy spectrum. These events have a higher probability to pass through the surface layer.	26
3.12	(a) Am-241 low energy spectrum from simulation before applying the best fit T-function charge collection efficiency. (b)Am-241 low energy spectrum from simulation after applying the best fit T-function charge collection efficiency. Most of the events above 14 keV move to the region under 14 keV. Spectrum (b) is almost 10 times higher than spectrum (a).	28
3.13	The best fit after applying T-function on Am-241 simulation data. With dead layer depth = 0.16, surface layer depth = 0.86 and $\alpha = 2.0$. Standard deviation of two spectra from 2.5 keV to 13.5 keV is 20.03.	29
3.14	(a) Cs-137 low energy spectrum from simulation before applying the best fit T-function charge collection efficiency. (b)Cs-137 low energy spectrum from simulation after applying the best fit T-function charge collection efficiency.	30



3.15	We are applying the exactly same T-function on Cs-137 simulation data. The standard deviation of two spectra from 2.5 keV to 13.5 keV is 58.80.	31
3.16	Charge collection efficiency $\varepsilon(x) = 0.5 - \tanh(11(0.51 - x))$. This function approach 0(smaller than 0.0005) when the depth x reach 0.16 mm, and approach 1 (greater than 0.9995) when the depth reach 0.86 mm.	32
3.17	Hyperbolic tangent charge collection efficiency applies to Am-241 low energy surface spectrum from simulation, measurement and simulation data start to separate below 5 keV. The standard deviation of two spectra from 2.5 keV to 13.5 keV is 38.98.	33
3.18	Hyperbolic tangent charge collection efficiency applies to Cs-137 low energy surface spectrum from simulation, measurement and simulation data start to separate below 2.5 keV. The standard deviation of two spectra from 2.5 keV to 13.5 keV is 47.23.	34
4.1	A typical waveform with some relevant parameters.	37
4.2	A saturated event which will be eliminated because the energy information is missing.	38
4.3	A multi-peaked noise event.	39
4.4	The relation between pedestal and amplitude, only events located in red lines will be considered in further analysis.	40



4.5	Relation between charge and amplitude, only events located in red lines will be considered in further analysis.	41
4.6	A 2-dimensional distributional of the time difference between Ge trigger and the last hit in cosmic ray veto panels versus the energy deposited in the Ge crystal, we can clearly see a strong concentration in a single band.	42
4.7	The spectra before and after applying the CRV criteria.	43
4.8	A 2-dimensional distribution of NaI(Tl) signal pulse amplitude versus energy deposit in Ge detector, events outside the signal band (red lines) should be eliminated.	44
4.9	The spectra before and after applying the ACV criteria.	45
4.10	(a) A spectrum after applying CRT and ACV criteria. Most of these events are cosmic ray induced neutron events in shielding. We need to correct the spectrum because of the detection efficiency of cosmic ray veto system, and the peaks around 10 keV are from Ge crystal. (b) A spectrum after applying CRV and ACT criteria. Most of these events are gamma events produced in shielding. We need to correct the spectrum again because of the detection efficiency of cosmic ray veto system.	46
5.1	A typical Germanium detector low energy VrV (CRV+ACV cut, after correction) spectrum, including several K/L shell peaks and background.	48



5.2	Decay chain for Uranium-238 and Thorium-232 series.	50
5.3	The location of X-ray lines in low energy VrV spectrum from a 500g n-PCGe detector.	53
5.4	3H production cross section vary from different Ge isotopes and neu- tron kinetic energy.[5]	54
5.5	3H beta decay spectrum and the end point around 18.6 keV depend on the mass of electron antineutrino. Plot on the right side is the end point zoom, blue line and red line means the electron antineutrino mass = $1 eV/c^2$ and mass = $0 eV/c^2$ respectively.[7]	55
5.6	The result of the 3H decay rate estimation. Magenta line is the 3H decay spectrum, and the red line is a fitting line formed by 3H decay spectrum + flat photon background + Gaussian peaks. The 3H decay spectrum indicates the decay rate upper limit is $32.5 kg^{-1} day^{-1}$. . .	57



List of Tables

5.1	The production rates of Cosmogenic nuclides at sea level using different cosmic neutron spectra.	51
5.2	These radionuclides are observed in the low energy VrV spectrum; they were produced in Ge crystal because of exposure to the cosmic ray neutron.	53



Chapter 1

Overview

1.1 TEXONO Overview

Taiwan EXperiment On Neutrino (TEXONO) collaboration was founded in October 1997 by pioneer scientists from Taiwan, Mainland China, and the United States. The main purpose of forming TEXONO is to start an experimental program of Neutrino and Astroparticle Physics in Taiwan. After several years of effort, TEXONO has published some quality papers. Middle East Technical University (METU), Turkey, have joined TEXONO Collaboration in the year 2004 while Banaras Hindu University (BHU), India joined in the year 2006.

The Kuo-Sheng Neutrino Laboratory (KSNL) is the main laboratory of TEXONO, which has been built up in the year 2001 and still operating. KSNL is located near a nuclear reactor, using High Purity Germanium (HPGe) Detector to study

low energy neutrino properties and dark matter searches. From improving electronic modules and the new generation HPGe detectors, TEXONO is looking forward to acquiring better experiment results.

1.2 A Brief Introduction to Neutrino

We can hardly notice the existence of neutrino even it does exist in the universe and pass through the Earth every day. Neutrino is a fundamental particle with half-integer spin, the electric charge is 0 and not affected by the strong force or electromagnetic force, only interact via weak interaction and gravity. However, gravity is weak in subatomic scale. Neutrinos are now one of the only founded candidates for dark matter.

Neutrino has three different flavors: electron neutrinos ν_e , muon neutrinos ν_μ and tau neutrinos ν_τ , they were labeled after being the partner of charged leptons (electron, muon, and tau) in charged-current weak interaction. During propagation, the three different flavor of neutrino will oscillate periodically to other flavors of neutrino, and this is a well-known phenomenon we call neutrino oscillation. This three neutrino flavor eigenstates can form an orthonormal basis, and so do the mass eigenstates ν_i , $i = 1, 2, 3$. These two bases are connected by PMNS (Pontecorvo—Maki—Nakagawa—Sakata) matrix, which is a unitary matrix.



$$\begin{bmatrix} \nu_e \\ \nu_\mu \\ \nu_\tau \end{bmatrix} = \begin{bmatrix} U_{e1} & U_{e2} & U_{e3} \\ U_{\mu1} & U_{\mu2} & U_{\mu3} \\ U_{\tau1} & U_{\tau2} & U_{\tau3} \end{bmatrix} \begin{bmatrix} \nu_1 \\ \nu_2 \\ \nu_3 \end{bmatrix}$$

Therefore, for a given flavor of neutrino, it is superposed by three different states of the neutrino with the different mass. The neutrino oscillation also implies that the neutrinos have finite masses.

1.3 A Brief Introduction to WIMPs

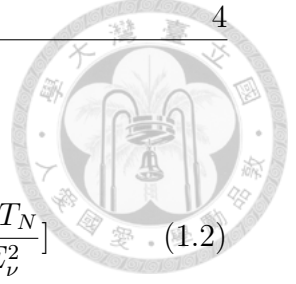
In the universe, about a quarter of the energy density is contributed by dark matter. As its name implies, the nature and properties of dark matter are still unknown. Weakly Interacting Massive Particle (WIMP) is one of the candidates for the unknown dark matter; they were produced in the early universe, calculation of the WIMPs abundance coincide the abundance of dark matter today, making WIMPs become the popular candidate of dark matter.

1.4 The Goal of TEXONO

1.4.1 Neutrino-Nucleus Coherent Scattering

Neutrino coherent scattering with the nucleus has never been experimentally observed. The interaction channel of this process is

$$\nu + N \longrightarrow \nu + N \quad (1.1)$$



and the cross section of this process is given by:

$$\left(\frac{d\sigma}{dT}\right)_{SM}^{coh} = \frac{G_F^2}{4\pi} m_N [Z(1 - 4\sin^2\theta_W) - N]^2 \left[1 - \frac{m_N T_N}{2E_\nu^2}\right] \quad (1.2)$$

$$\sigma_{tot} = \frac{G_F^2 E_\nu^2}{4\pi} [Z(1 - 4\sin^2\theta_W) - N]^2 \quad (1.3)$$

where m_N is the mass of the nuclei, E_ν is the incident neutrino energy and T_N is the measurable recoil energy of the nucleus. This formula is eligible for $E_\nu < 50$ MeV. The nuclear power reactor provides a myriad of reactor neutrinos which are in the MeV range, for the maximum energy of reactor neutrino is about 8 MeV, the maximum nuclear recoil energy for Ge target is about 1.9 keV[1]. With an ultra low energy Ge detector, we are hoping to understand more about this process.

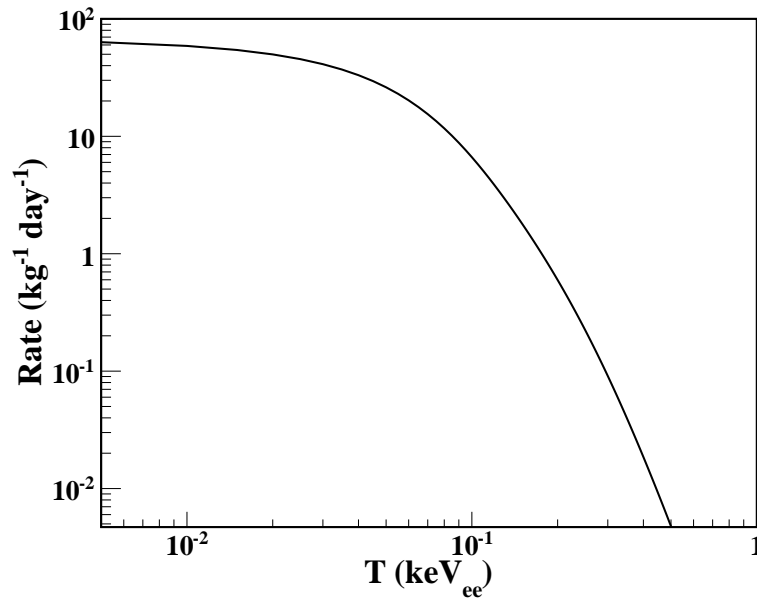
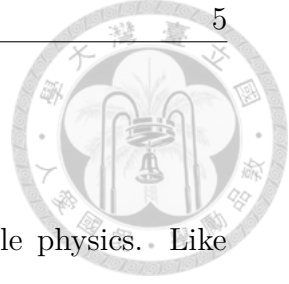


Figure 1.1: Expected integral $\bar{\nu}_e$ -N coherent scattering rates due to Standard Model contributions at the flux $\phi(\bar{\nu}_e) = 10^{13} \text{cm}^{-2} \text{s}^{-1}$, where “ee” denote electron-equivalent energy, assuming realistic detector resolution.



1.4.2 Dark Matter Searching

A direct detection of WIMP is a challenging task in astroparticle physics. Like neutrinos, WIMPs will interact with matter via coherent scattering mechanism:



where WIMPs are denoted by χ . With sub-keV sensitive Ge detector, we optimize to probe “light” WIMPs with m_χ about 1-10 GeV. Therefore, to lower the background level and lower the detector threshold is required.

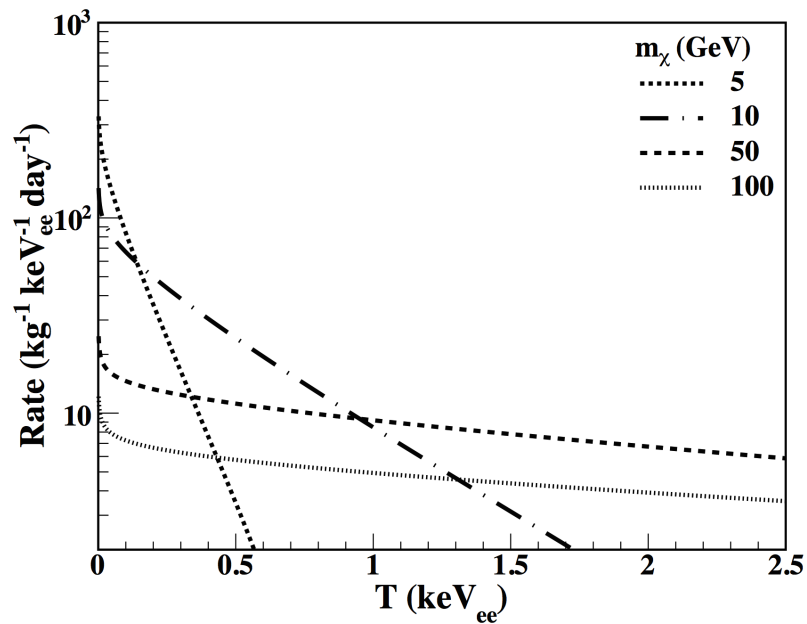


Figure 1.2: Recoil spectra for χ -Ge interactions at a crosssection of 10^{-40} cm^2 with different values of m_χ . Assuming an 1 kg-year data and background level at $1 \text{ kg}^{-1} \text{ keV}_{ee}^{-1} \text{ day}^{-1}$.



Chapter 2

Experimental Setup

2.1 Kuo-Sheng Neutrino Laboratory

To obtain an intense source of neutrinos, TEXONO built the neutrino laboratory at Kuo-Sheng Nuclear Power Plant, which was located in Wanli District, the northeast shore of Taiwan. This nuclear power plant was the second nuclear power plant in Taiwan. It consists of two boiling water reactor cores, the commission date of unit 1 and unit 2 was in December 1981 and March 1983, respectively, each with an average thermal output of 2.9 GW. The standard operation includes about 18 months of reactor ON followed by about 50 days of reactor OFF period when reactor fuel cells are replaced.

Kuo-Sheng Neutrino Laboratory (KSNL) is on the first floor of the seven-storey reactor building, at a distance of 28 m from the center of the core-I, and 102 m from the center of core-II. A schematic side view of the reactor building of nuclear power



plant and the experimental site is shown in Figure 2.1.

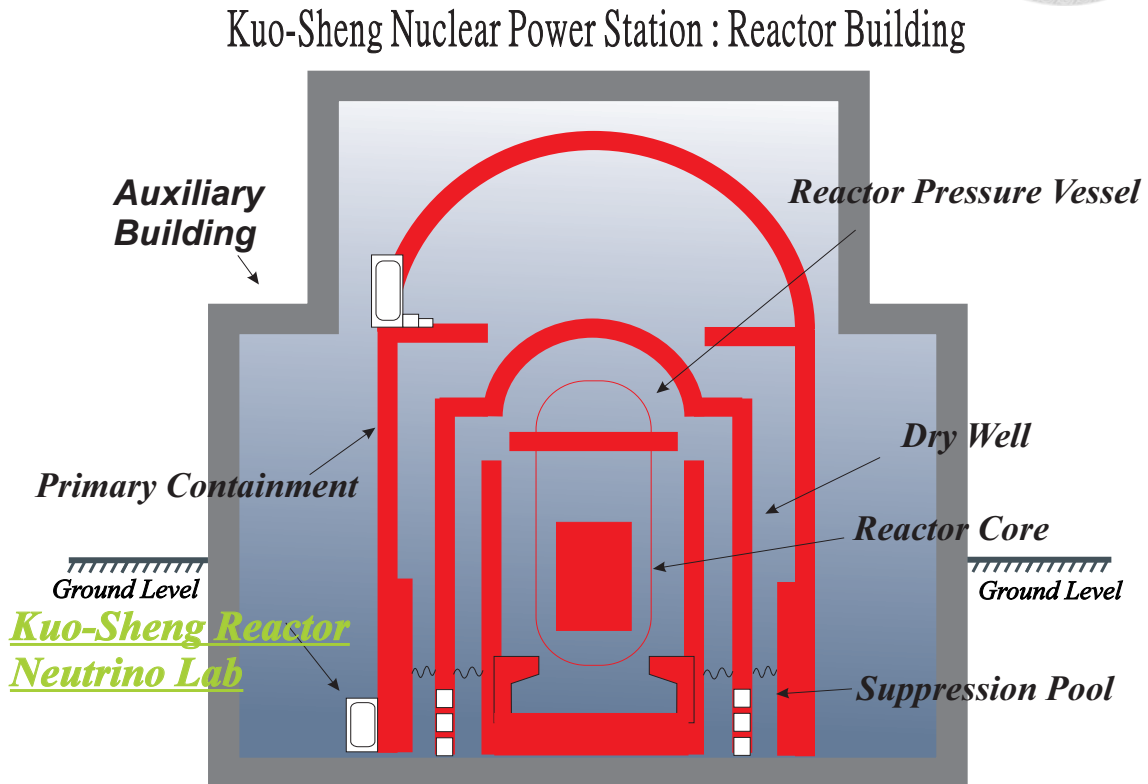


Figure 2.1: Schematic side view of the Kuo-Sheng nuclear reactor building, and relative location of the reactor core and KSNL site (not drawn to scale).

2.2 Shielding

The background level should be suppressed as hard as possible to obtain better results in the experiment. There are many different sources in KSNL site will raise the background level, like cosmic ray, fallout and some radionuclide in the build-

ing material (Some contributor of the background will be discussed in chapter 5). KSNL is located on the first floor of the reactor building, which is just slightly underground about 30-meter water equivalent (M.W.E), it is essentially not enough for the background source like cosmic ray, so we build up both passive shielding and active shielding to reduce the background.

2.2.1 Passive Shielding

The passive shielding for the experiment at KSNL is designed for multi-purpose, this passive shielding has a total weight of 50 tons, containing 4 layers for different purposes, and the dimension of the shielding inner space is $100\text{ cm} \times 80\text{ cm} \times 75\text{ cm}$, the shielding structure is depicted in Figure 2.2 schematically.

Each layer is made from different material and designed for different purposes, they are, from the outermost layer:

- (i) A 15 cm thick low activity Pb, to block the ambient photons. To block the ambient photons, the ideal thickness of Pb is around 10-15 cm, any Pb thicker than 15 cm will become a significant source of muonic-induced bremsstrahlung and secondary neutrons. For photons above 1 MeV, less than 0.05% of them can penetrate the lead shielding, and even fewer photons with energy below 1 MeV can penetrate the lead shield. Because for photon energy above 1 MeV, the photon attenuation length in the lead is about 2 cm for a two MeV photon, and photon attenuation length is about 10 cm for photon energy greater than 100 MeV; this value drops severely for photon energy less than 1 MeV.
- (ii) A 5 cm stainless steel frame to support the structures, and further reduced

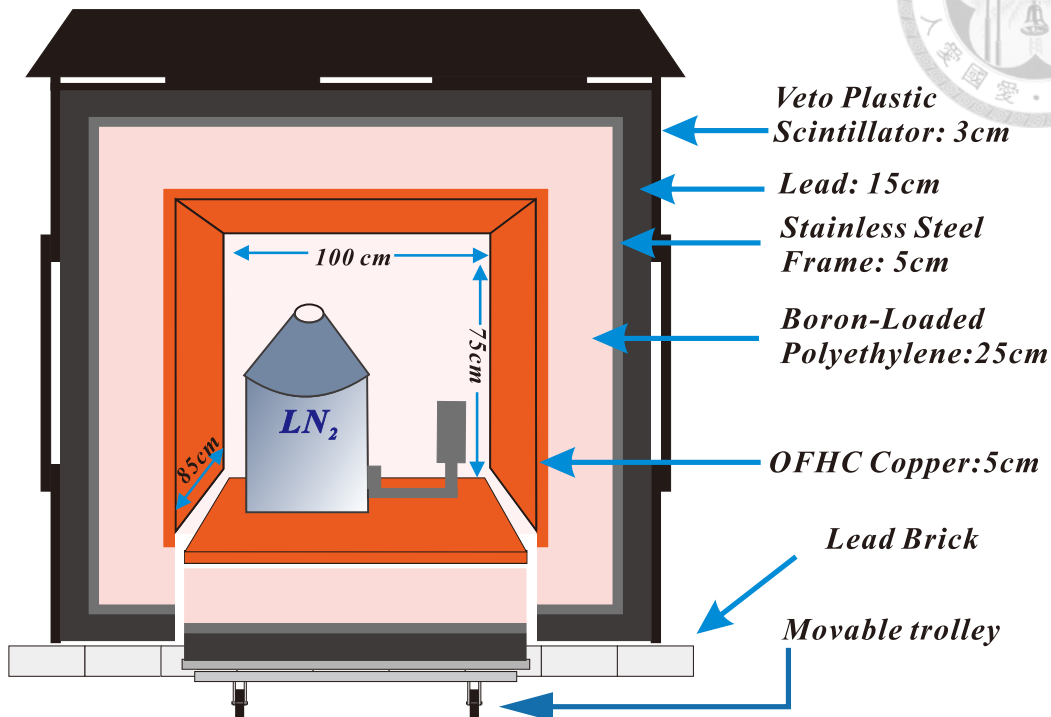


Figure 2.2: The shielding design for KSNL, including the shielding material and the dimension of each layer.

the γ -ray flux. The main component of the stainless steel is iron, which is good to absorb thermal neutrons, and slowing down fast neutrons by inelastic scattering.

- (iii) A 25 cm boron-loaded polyethylene to absorb the cosmic ray induced neutrons in lead and steel.
- (iv) A 5 cm oxygen-free high conductivity (OFHC) copper to absorb the photons from intrinsic radioactive contamination. The excited state of nuclei induced by neutron or cosmic ray in lead and polyethylene, the photons produced

from de-excitation are expected to be lower than 2.6 MeV, and over 90% of the photons in MeV range can be absorbed by OFHC copper. For most of the background photons, the energy is lower than 1 MeV, and over 99% of them can be absorbed by copper.

2.2.2 Active Shielding

For the cosmic ray in KSNL, most of them are the muonic components, while the hadronic components are blocked by the 30 M.W.E overburden on top of the reactor building. To lower the background level, building an active shielding to handle these cosmic ray muonic components is necessary. Therefore, we construct a cosmic-ray veto system. This system consists of 16 pieces of 3 cm thick plastic scintillators. The plastic scintillators cover each side of the passive shielding except the bottom side, the detection efficiency of plastic scintillators to muon flux is around 92%, about 8% of the cosmic ray muons will be missed due to a small space. This space is left for installing the photomultiplier tube(PMT)s at the upper end of front side as well as the backside. We can categorize the plastic scintillators into three groups by their dimensions and PMT configuration,

- (i) 4 plastic scintillators of dimensions $3\text{ m} \times 1\text{ m} \times 3\text{ cm}$ are placing on the top of the shielding, we install 2 PMTs at both sides of each plastic scintillator(4 PMTs for each plastic scintillator at top side).
- (ii) At both the left and right side, 3 plastic scintillators of dimensions $3\text{ m} \times 1\text{ m} \times 3\text{ cm}$ are placed, we install 1 PMT at both sides of each plastic scintillator(2 PMTs for each plastic scintillator at the left and right side).

- (iii) At both the front and back side, 3 plastic scintillators of dimensions $1.5\text{ m} \times 1\text{ m} \times 3\text{ cm}$ are placed, we install 2 PMTs at the top side of each plastic scintillator (2 PMTs for each plastic scintillator at the front and back side).

The schematic layout of the cosmic ray veto plastic scintillators is depicted in Figure 2.3, and the photograph of the plastic scintillators with the arrangement of the PMTs at the front side are shown in Figure 2.4.

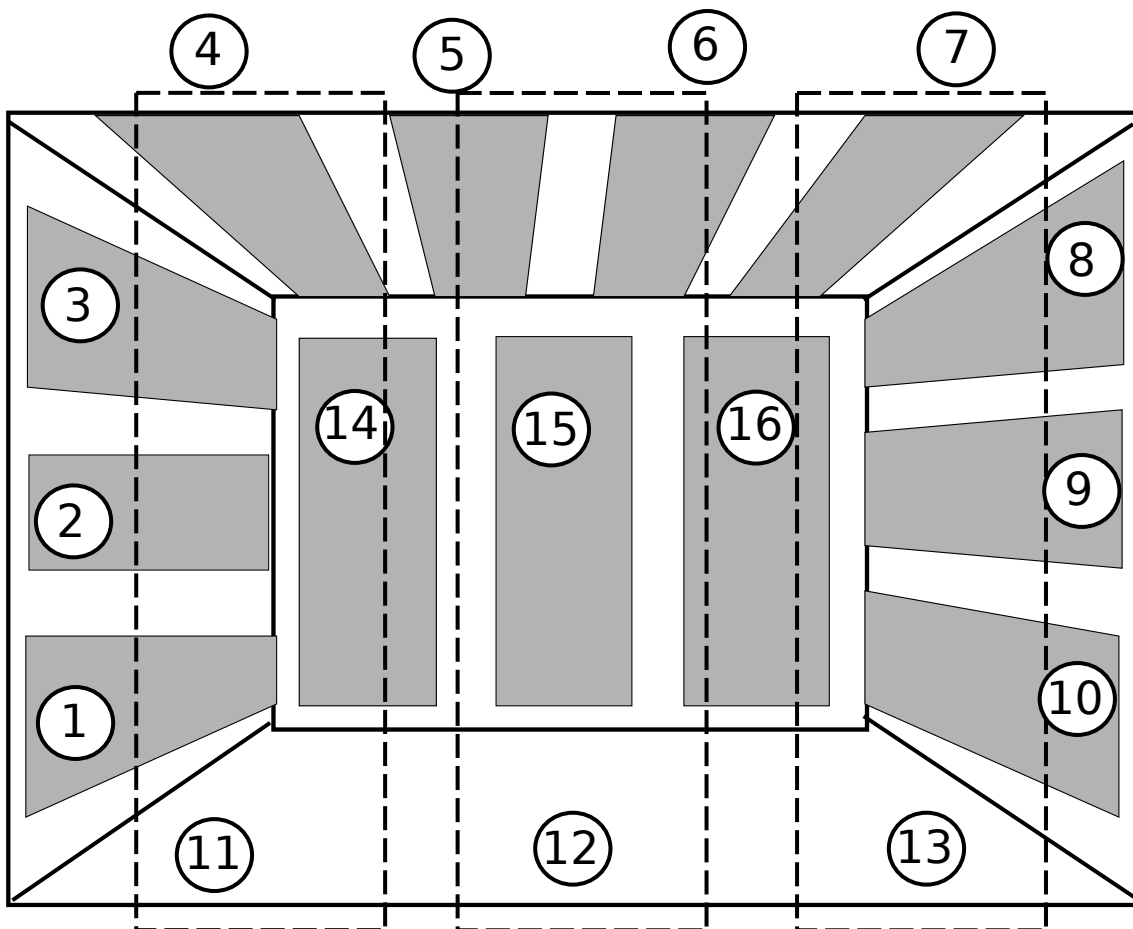


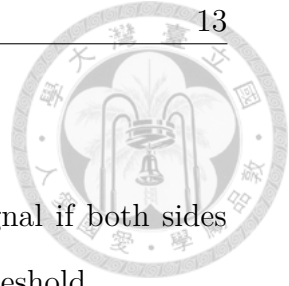
Figure 2.3: Schematic layout of the 16 cosmic ray veto plastic scintillators.



Figure 2.4: Photograph of the plastic scintillators (the black panels) at the front side and their attached PMTs on upper ends.

The top side of the cosmic ray veto system is relatively important to the other sides because most of the cosmic ray muons are coming from the top side. Therefore, we design three different logics employ on each top PMTs signal to avoid noise from PMT itself:

- (i) 2/4 Logic: we will qualify an event as cosmic ray signal if there are two or



more PMT signals above the threshold.

- (ii) Both Side Logic: we will qualify an event as cosmic ray signal if both sides (left and right side) of the PMTs have a signal above the threshold.
- (iii) Q-Logic: we will qualify an event as cosmic ray signal if the voltage (amplitude) and charge (area) of each PMT signals satisfy the thresholds indicate a cosmic ray signal.

The output signals will then send to the discriminator; a global threshold is applied to all discriminators.

The event rate of the cosmic ray veto detector is about 5 kHz, the top 4 plastic scintillators with a total area of $12 m^2$ contribute 2 kHz to event rate, and 1 kHz are contributed by the rest of the plastic scintillators. The remaining 2 kHz are coming from surrounding gamma background and electronic noise of PMTs.

The signals coming from the cosmic ray veto detector are not used to reject the trigger from HPGe detector on-line. Some information from these cosmic ray events are needed, we will save the energy information and the time difference between the HPGe trigger and the veto signal. During off-line data analysis, instead of just remove the events recorded in cosmic ray veto detector, we will inspect these events. If any of these events qualify some conditions which were set by us, it will be considered as a cosmic ray or the induced events; then these events will be removed to lower the background. The event selection is optimized without throwing away too many candidate events in the off-line analysis.

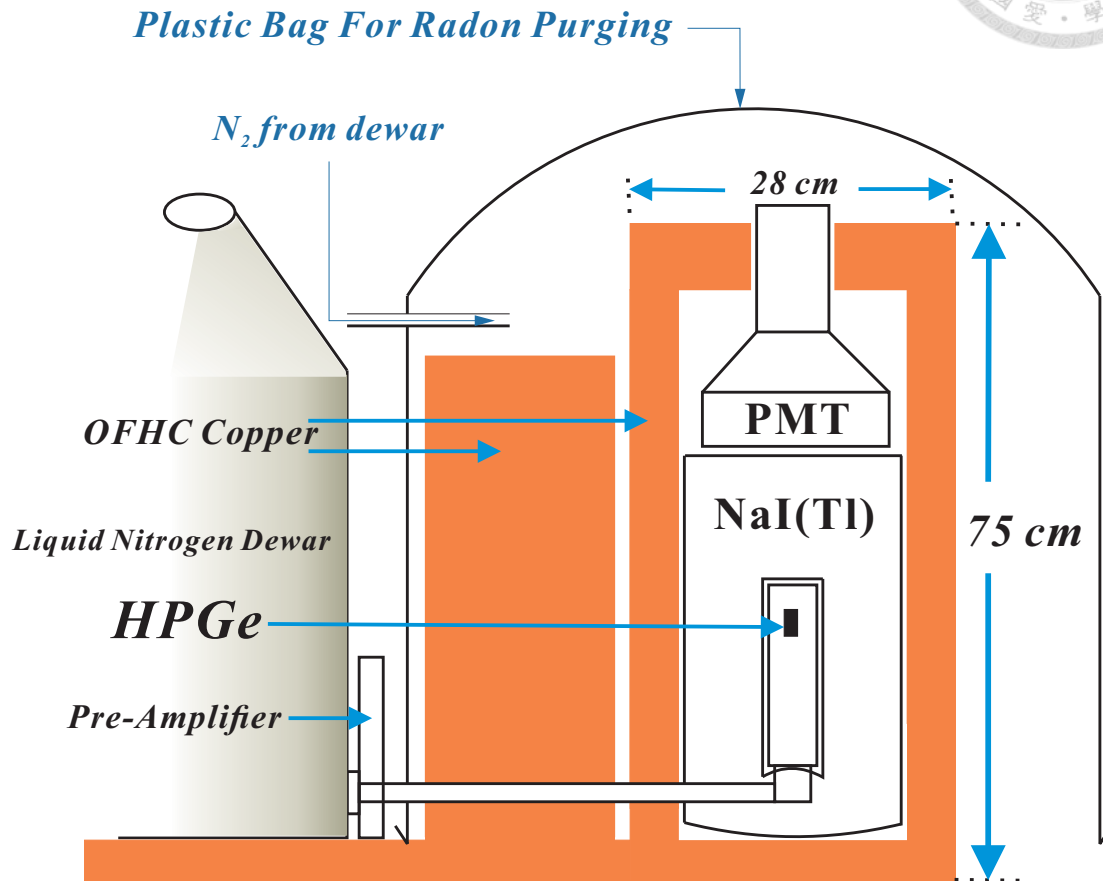
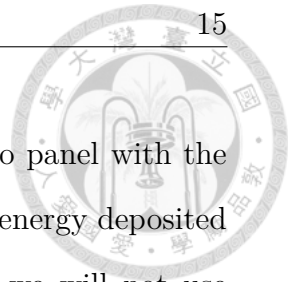


Figure 2.5: Schematic side view of the set up inside the passive shielding.

In KSNL, we place an anti-Compton detector to be our second active shielding inside the passive shielding. TEXONO Collaboration chooses NaI(Tl) detector due to its excellent energy resolution, threshold and high detection efficiency for various radiation. The drawback is that the NaI(Tl) crystal contain a small amount of contamination of natural potassium, it is less than 0.5 ppm by weight, and have a single gamma ray emission from ^{40}K at 1460.83 keV. With a 5 cm thick NaI(Tl)

crystal, it provides more efficient suppression than cosmic ray veto panel with the threshold of 20 keV. It also provides the time information and the energy deposited in NaI(Tl) crystal. Like signals from cosmic ray veto detector, we will not use the NaI(Tl) detector signals to reject the trigger from HPGe detector on-line, but handle these events during off-line data analysis. A schematic side view of the set up inside the passive shielding is shown in Figure 2.5, including HPGe detector, NaI(Tl) detector, and some OFHC copper bricks.





Chapter 3

The Surface Effect of p-type Germanium Detector

3.1 p-type Point Contact Germanium Detector

3.1.1 Germanium Detector Configuration

There are several configurations of the Ge detector, we used standard electrode semi-coaxial Ge detector(SEGe) many years ago, then we switched to the point contact germanium detector(PCGe), the biggest advantage of PCGe is that the capacitance is reduced by large factor compare to SEGe.

The capacitance is around 20pF for SEGe and less 1pF for PCGe. We can receive some benefit from lower capacitance:

- (i) The noise fluctuation is reduced.

- (ii) The energy resolution is improved because of the reduction of noise fluctuation. The energy resolution is decided by statistical effects, incomplete charge collection, and noise fluctuation.

$$(\Delta E_{total})^2 = (\Delta E_{stat})^2 + (\Delta E_{icc})^2 + (\Delta E_{noise})^2$$

- (iii) The timing resolution is improved, allowing us to identify some of the double hit events in the crystal.
- (iv) The energy threshold is improved, the threshold is 2-5 keV for SEGe and 300-400 eV for PCGe.

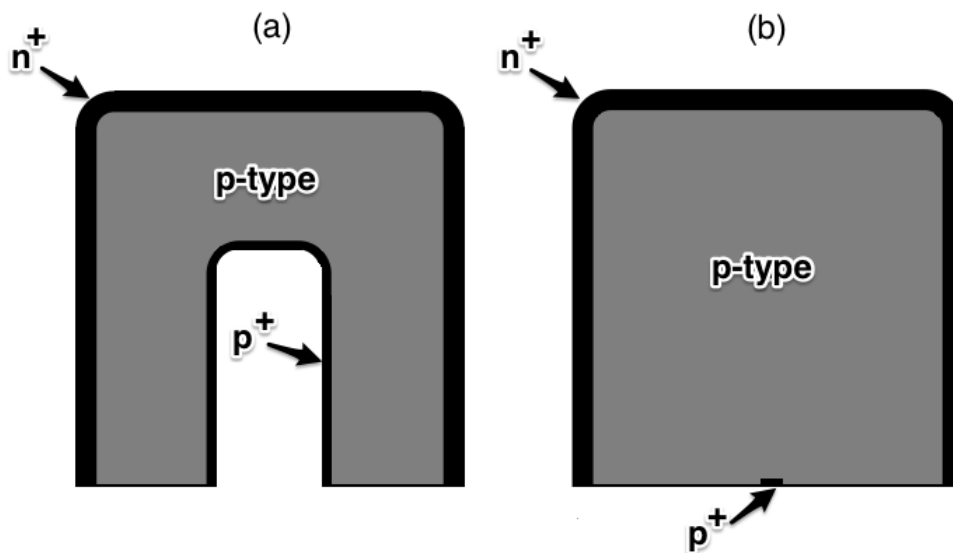


Figure 3.1: (a) P-type semi-coaxial germanium detector, the p contact in this configuration is cylindrical. (b) P-type point contact germanium detector, the capacitance is lower in this configuration because the p contact shrink to a tiny disk (about 5 mm in diameter).

We are using two different configurations of point contact Ge detector. The p-type point contact germanium detector (P-PCGe) and n-type point contact germanium detector (N-PCGe). The outer contact of N-PCGe is a thin, ion-implanted p^+ contact; for P-PCGe, the outer contact is a thick, lithium n^+ contact.

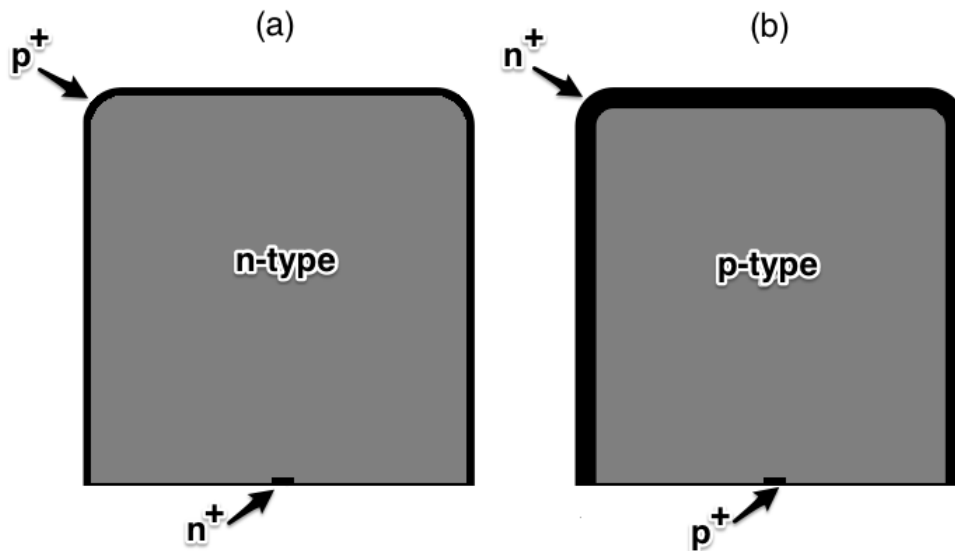


Figure 3.2: (a) N-type PCGe which have a thin, ion-implanted p^+ outer contact. (b) P-type PCGe which have a thick, lithium n^+ outer contact.

3.1.2 Surface Layer

The p-type point contact germanium detector has an inactive thick lithium n^+ for its outer contact. We can control the depth by controlling the amount of lithium diffuse into this region. We call it dead layer because the charge collection efficiency ϵ is zero in this region, which means the energy deposited in this region will not

present in the energy spectrum. There is another region we call it transition layer between the dead layer and the active bulk (charge collection efficiency $\varepsilon = 1$). The charge collection efficiency ε is a function of depth in transition layer, for the dead layer and transition layer, we collectively called surface of the p-PCGe detector.

There are several different profiles of the function we can assume in transition layer, such as (1) hyperbolic tangent, (2) sigmoid function and (3) T-function,

$$\begin{aligned}
 (1) \quad \varepsilon(x) &= 0.5 - 0.5 \tanh(Ax - B) \\
 (2) \quad \varepsilon(x) &= \frac{1}{1 + Ae^{-B(x-d_{sl})}} \\
 (3) \quad \varepsilon(x) &= \begin{cases} 0 & \text{if } 0 \leq x < d_{dl} \\ 2^{\left(\frac{x-d_{dl}}{d_{sl}-d_{dl}}\right)^\alpha} - 1 & \text{if } d_{dl} \leq x \leq d_{sl} \\ 1 & \text{if } x > d_{sl} \end{cases}
 \end{aligned}$$

where x is the depth measured from the outer lithium contact, d_{sl} is the width of the surface layer, d_{dl} is the width of the dead layer and α is the concavity of the function. The parameter A and B can be determined by finding the best fit of simulation and measurement data.

The surface structure schematic diagrams of the p-PCGe detector for three different charge collection efficiency functions are depicted in Figure 3.3-3.5.

In p-PCGe detector, we can distinguish surface and bulk event by examining the rise time of the pulse. Because the electric field is weak in transition layer, only part of the carriers generated in transition layer can reach the bulk, and carriers in transition layer move slower than the carriers in bulk. So we will lose some energy

information in transition layer and the rise time in transition layer is longer than the rise time in bulk.

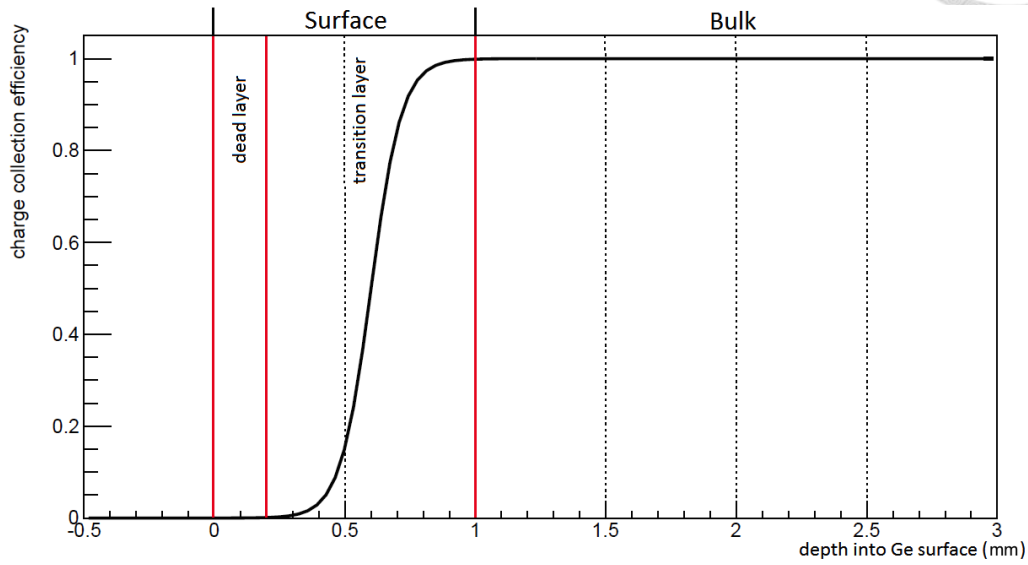


Figure 3.3: (a) Hyperbolic Tangent. The structure of the charge collection efficiency in an 1 mm surface layer with using hyperbolic tangent.

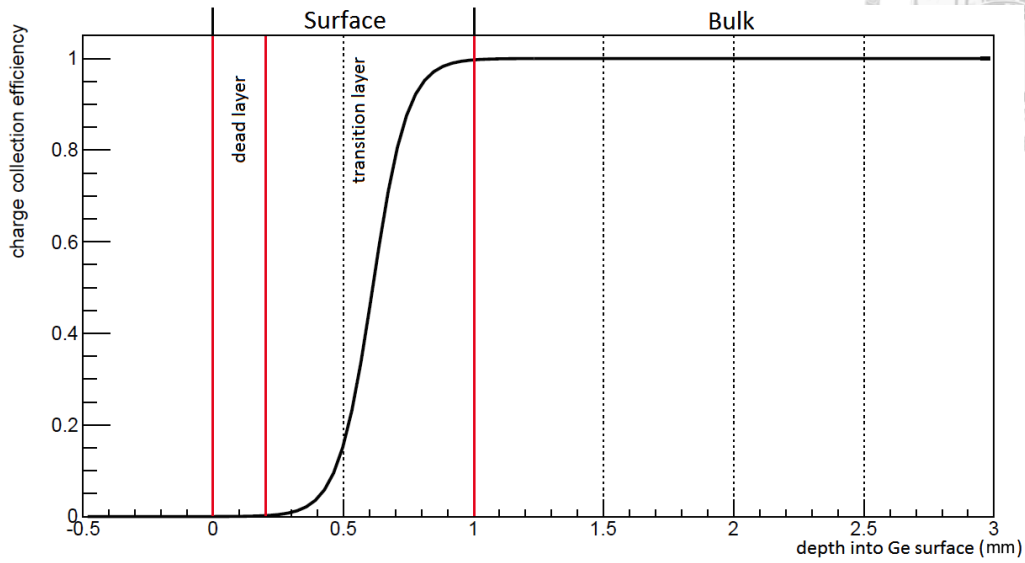


Figure 3.4: (b) Sigmoid Function. The structure of the charge collection efficiency in an 1 mm surface layer with using sigmoid function.

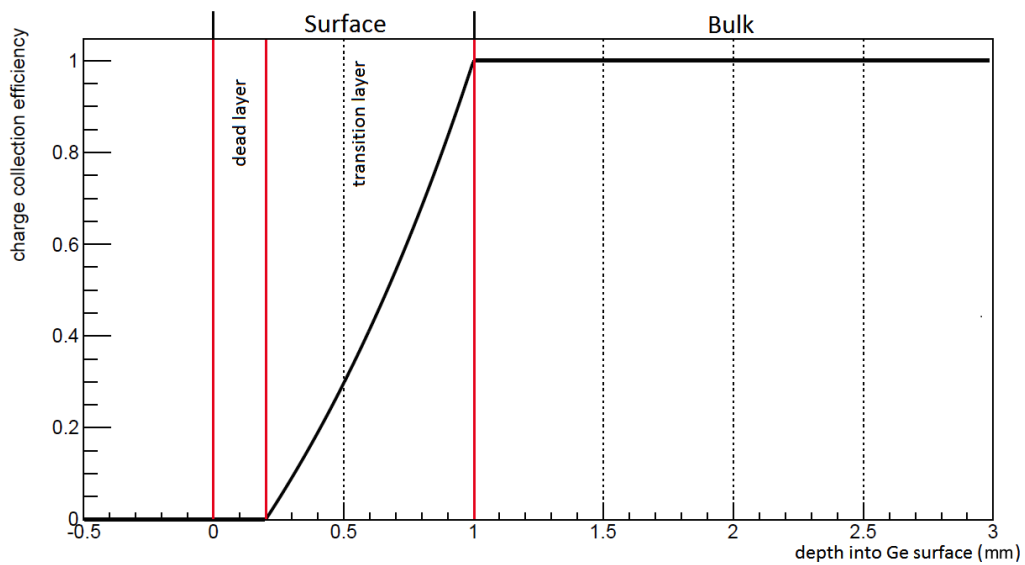


Figure 3.5: (c) T-function. The structure of the charge collection efficiency in an 1 mm surface layer with using T-function.

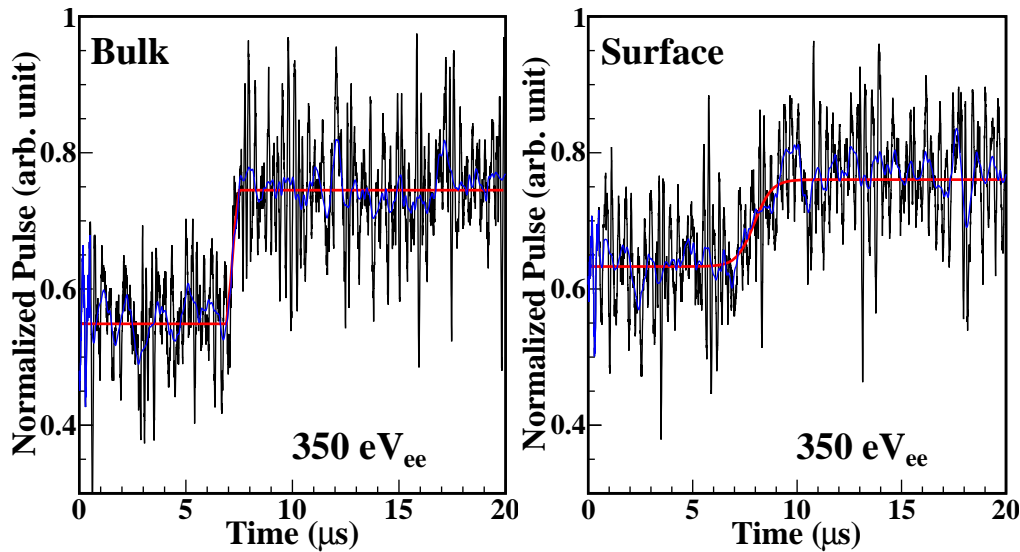


Figure 3.6: The pulse for bulk(left side) and surface(right side) near threshold, the rise time of the surface pulse is longer.

There are two main advantages of the p-PCGe. First is the dead layer will act as a shield and block the external low energy radiation below around 60keV, second is that the energy resolution is better than n-PCGe, the majority charge carrier in n-PCGe is electron which tends to trap by impurities in Ge crystal.

The disadvantage of p-PCGe is that the energy deposit in transition layer cannot be fully absorbed. For example, a 100 keV energy deposit in transition layer with the depth correspond to 20% charge collection efficiency, what we record this event in energy spectrum will become 20 keV instead of its real energy 100 keV. This information loss will result in a higher count in low energy region compare to n-PCGe, and the event in low energy region is difficult for us to distinguish whether it is a surface event or a bulk event.

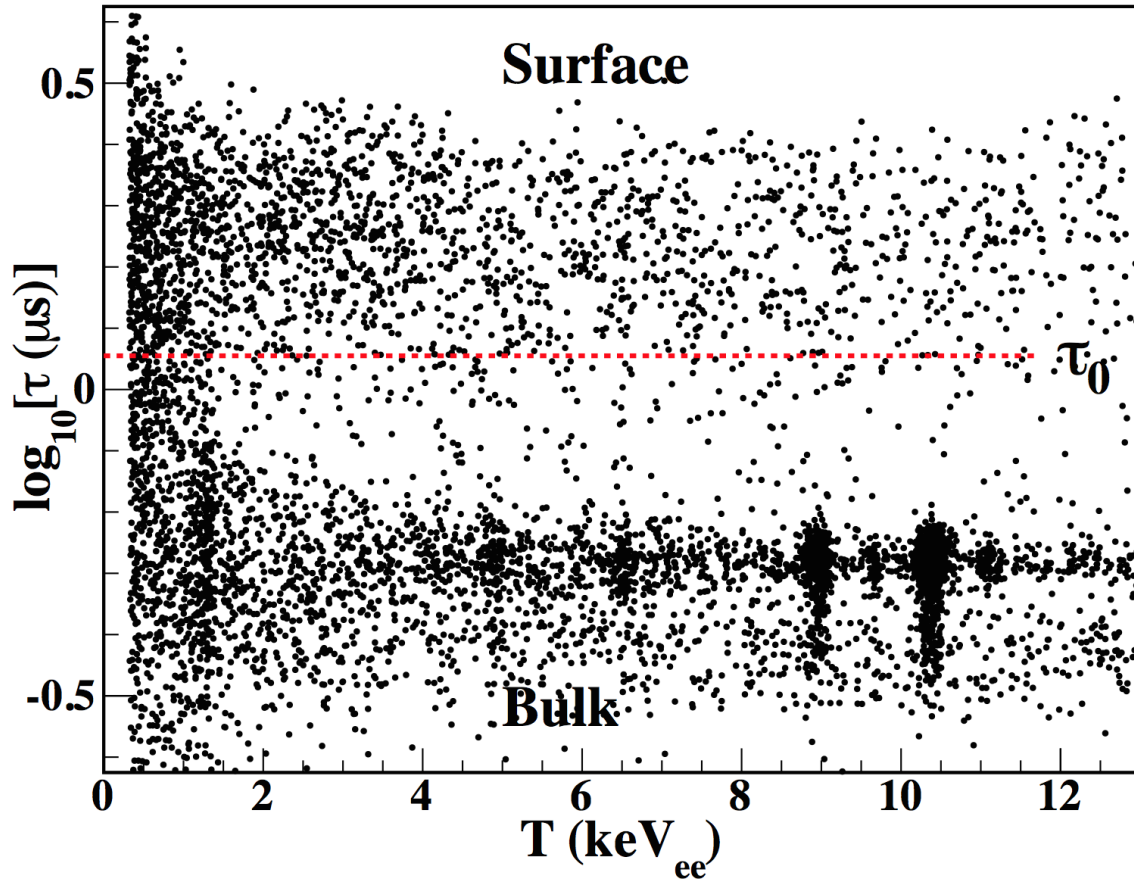


Figure 3.7: In log rise time vs. energy plot, we can clearly see that for energy greater than 2 keV, it is easy for us to distinguish surface and bulk events because the events are divided, but the events below 2 keV are mixed and difficult for us to distinguish.

3.2 Charge Collection Efficiency in Transition Layer

In transition layer, charge collection efficiency is a function of depth, we have some unknown constants in the function which can be determined by finding the best fit of simulation and measurement data. In this chapter, we will try to find the unknown constants in hyperbolic tangent profile and T-function profile.

3.2.1 Simulation and Measurement Data Taking Environment

(1)Simulation:

For generating the simulation data, we use a Monte Carlo simulation software called GEANT4(GEometry ANd Tracking) which was developed by CERN. In GEANT4, we simply set up a 900g p-PCGe detector which is similar to our real 900g p-PCGe detector and then generate events at the top of the detector. We distribute these events on a disk at the top of the detector, and the direction for every generated event are traveling in -z direction.

(2)Measurement:

We measure the data in our laboratory at Academia Sinica, and separate the data taking process into two parts.

First, we put the Am-241 or Cs-137 source on the top of 900g p-PCGe detector copper shell, then start the data taking. After a period, we can get the energy spectrum.

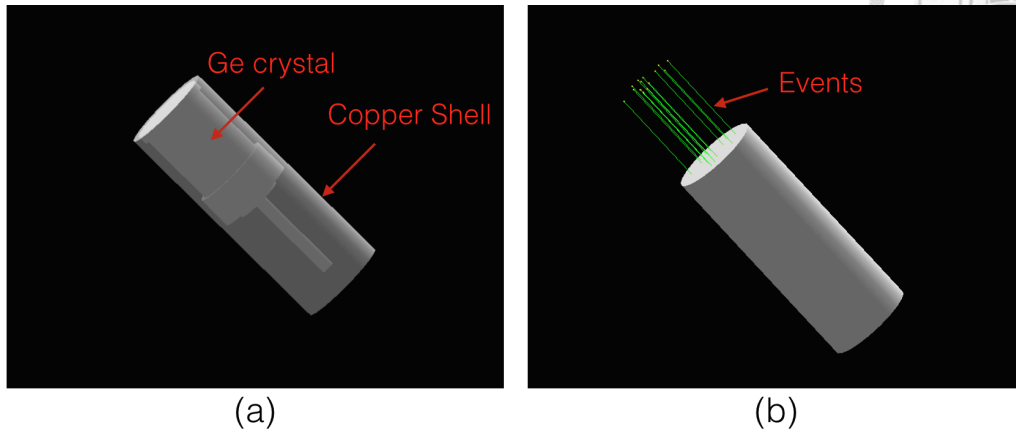


Figure 3.8: (a) The geometry of 900g p-PCGe detector in GEANT4. (b) Events starting points are distributed on a disk at the top of the detector, and traveling in $-z$ direction.

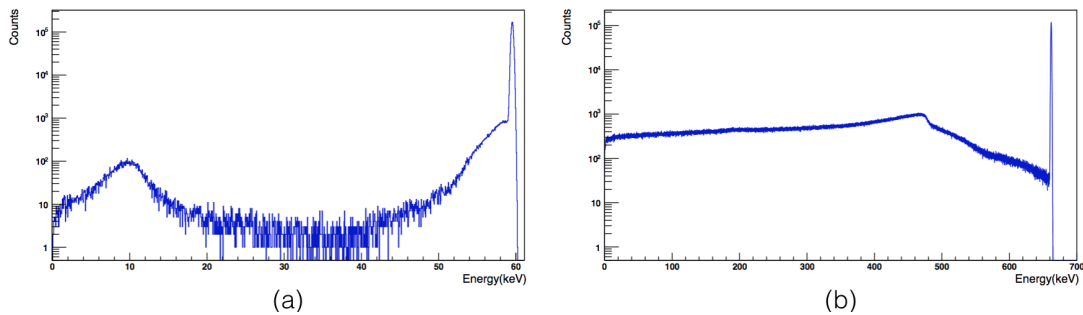


Figure 3.9: (a) Am-241 energy spectrum simulated by GEANT4. (b) Cs-137 energy spectrum simulated by GEANT4.

Second, we take the Am-241 or Cs-137 source away, then start the data taking. We can get the background spectrum. After normalizing the background spectrum, we subtract the background from Am-241 and Cs-137 energy spectrum.

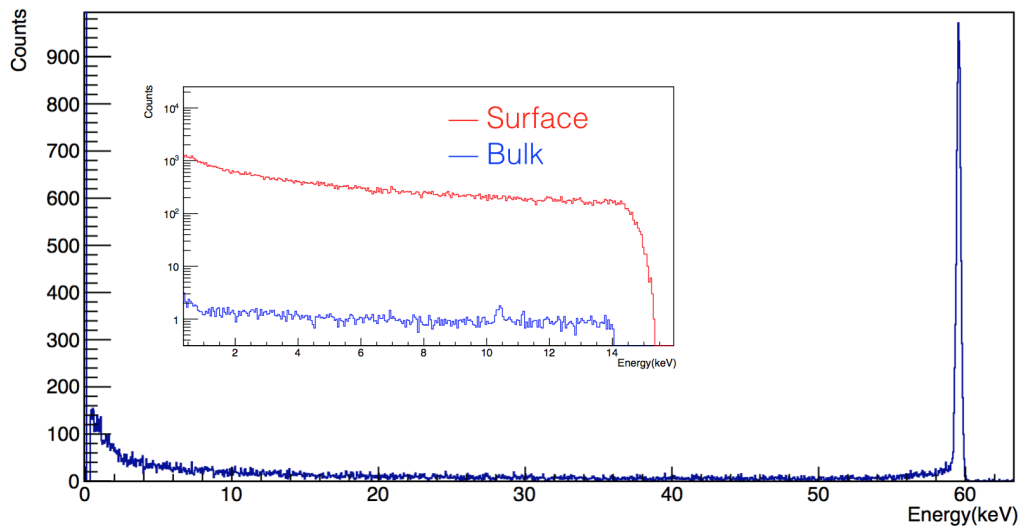


Figure 3.10: The measurement of Am-241 high energy and low energy spectrum. Most of the events are stopped and deposit their energy in the surface.

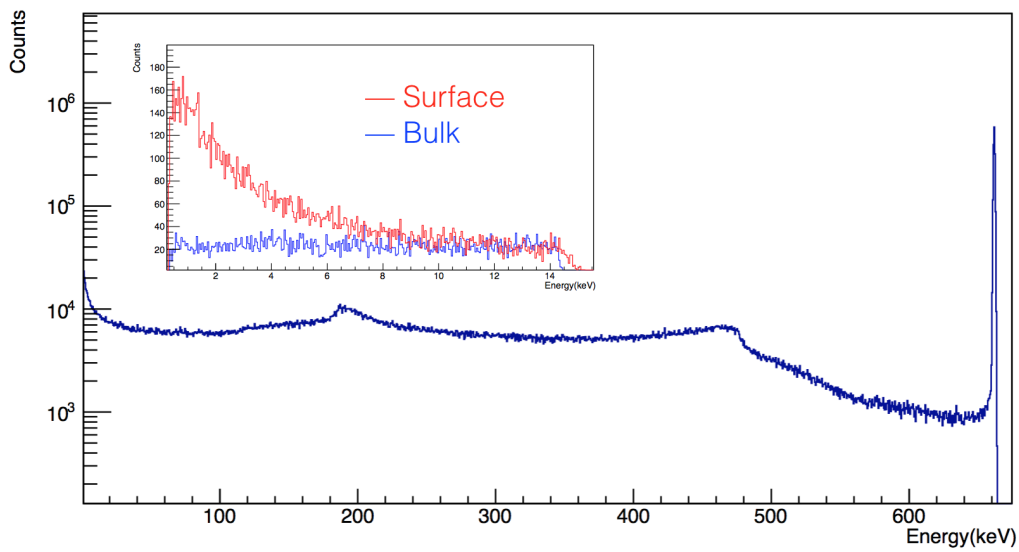
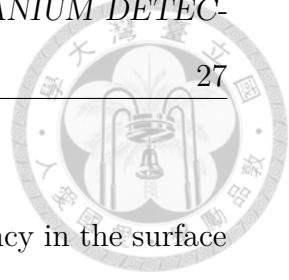


Figure 3.11: The measurement of Cs-137 high energy and low energy spectrum. These events have a higher probability to pass through the surface layer.



3.2.2 T-function Profile

T-function is a function we assume for the charge collection efficiency in the surface layer, there are three parameters we can adjust, including dead layer depth, surface layer depth and α to change the function's concavity.

$$T - function\ profile : \varepsilon(x) = \begin{cases} 0 & \text{if } 0 \leq x < d_{dl} \\ 2^{\left(\frac{x-d_{dl}}{d_{sl}-d_{dl}}\right)^\alpha} - 1 & \text{if } d_{dl} \leq x \leq d_{sl} \\ 1 & \text{if } x > d_{sl} \end{cases}$$

For finding the best fit of this function, we set the three adjustable parameters like:

1. Adjust the depth of dead layer from 0.1 mm to 0.3 mm.

$$\text{Dead layer depth} = 0.1 + 0.02 \times n \text{ mm, } n = 0, 1, 2, \dots, 10.$$

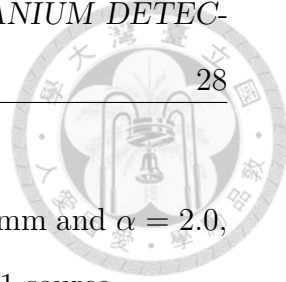
2. Adjust the depth of surface layer from 0.8 mm to 1.1 mm.

$$\text{Surface layer depth} = 0.8 + 0.02 \times n \text{ mm, } n = 0, 1, 2, \dots, 15.$$

3. Adjust α from 1.5 to 2.5.

$$\alpha = 1.5 + 0.1 \times n, n = 0, 1, 2, \dots, 10.$$

There are 1936 of combinations from the parameters we are setting above, using Am-241 to find the best fit of simulation and measurement low energy spectrum of the surface. First, we normalize the spectra of simulation and measurement to a same total number of events from 2.5 keV to 13.5 keV; second, calculate the standard deviation of two spectra from 2.5 keV to 13.5 keV. The best fit is defined by the smallest standard deviation in total 1936 of combination; the result is shown below.



When the depth of dead layer = 0.16 mm, surface layer = 0.86 mm and $\alpha = 2.0$, we get the best fit of simulation and measurement data for Am-241 source.

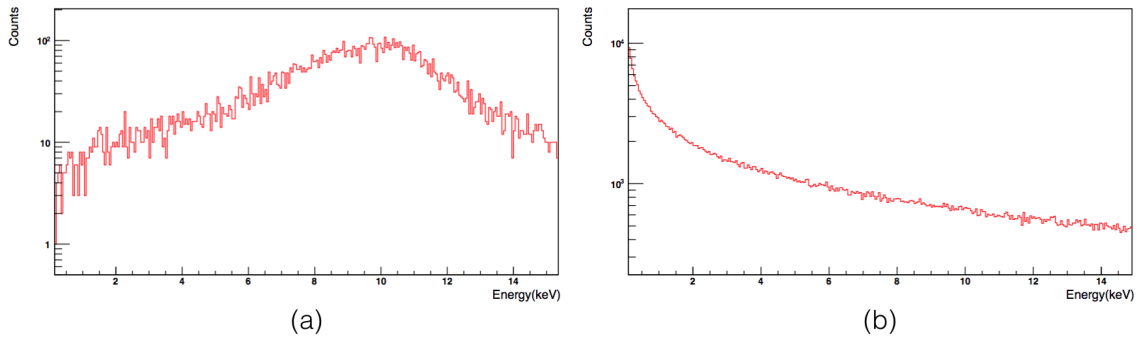


Figure 3.12: (a) Am-241 low energy spectrum from simulation before applying the best fit T-function charge collection efficiency. (b) Am-241 low energy spectrum from simulation after applying the best fit T-function charge collection efficiency. Most of the events above 14 keV move to the region under 14 keV. Spectrum (b) is almost 10 times higher than spectrum (a).

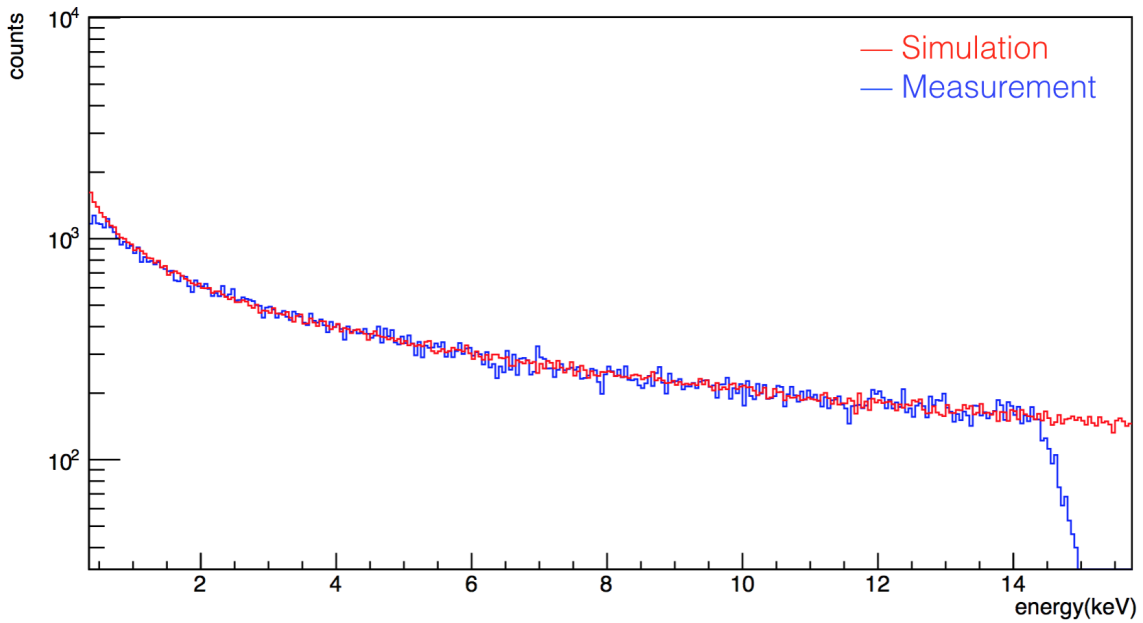


Figure 3.13: The best fit after applying T-function on Am-241 simulation data. With dead layer depth = 0.16, surface layer depth = 0.86 and $\alpha = 2.0$. Standard deviation of two spectra from 2.5 keV to 13.5 keV is 20.03.

We now applying the same charge collection efficiency function with same parameters on Cs-137, the Cs-137 simulation spectra before and after applying the T-function are shown in Figure 3.14, and the comparison between Cs-137 measurement and simulation are shown in Figure 3.15.

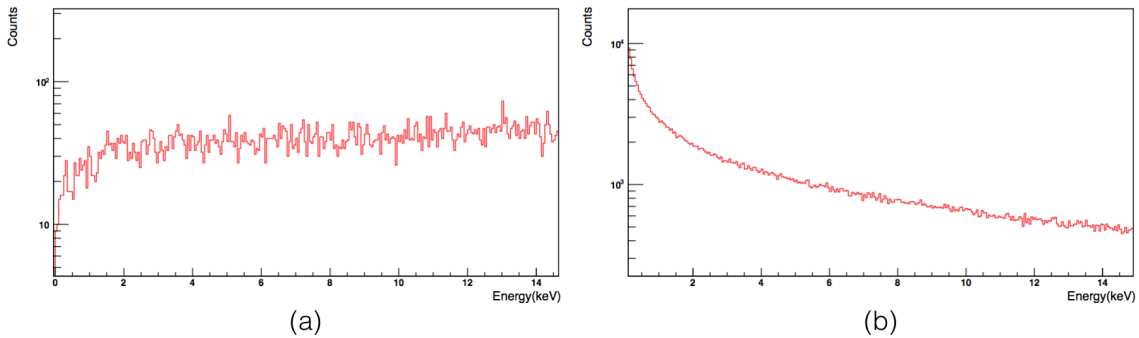


Figure 3.14: (a) Cs-137 low energy spectrum from simulation before applying the best fit T-function charge collection efficiency. (b)Cs-137 low energy spectrum from simulation after applying the best fit T-function charge collection efficiency.

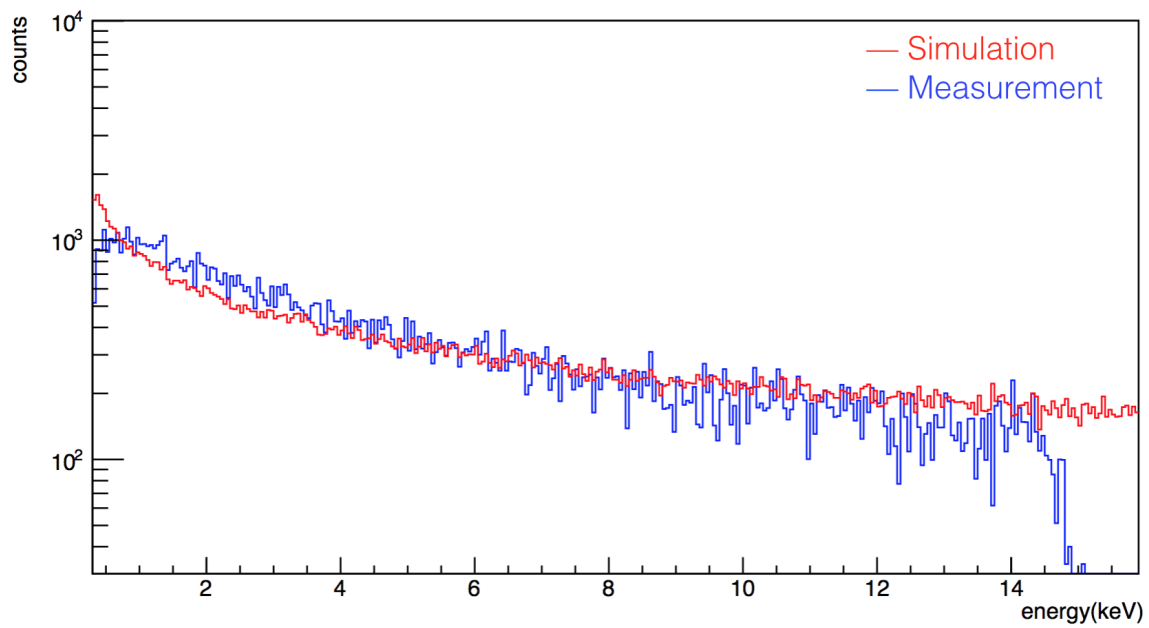


Figure 3.15: We are applying the exactly same T-function on Cs-137 simulation data. The standard deviation of two spectra from 2.5 keV to 13.5 keV is 58.80.



3.2.3 Hyperbolic Tangent Profile

Hyperbolic tangent profile : $\varepsilon(x) = 0.5 - 0.5 \tanh(Ax - B)$

Since we found the depth for the dead layer and surface depth by fitting T-function, we can apply the same depth in hyperbolic tangent profile. We adjust parameter A and B in hyperbolic tangent to let it approach 0 when the depth x reach 0.16 mm, and approach 1 when x reach 0.86mm(Figure 3.16). In this section, we can check that will a symmetrical function fitting better than T-function or not.

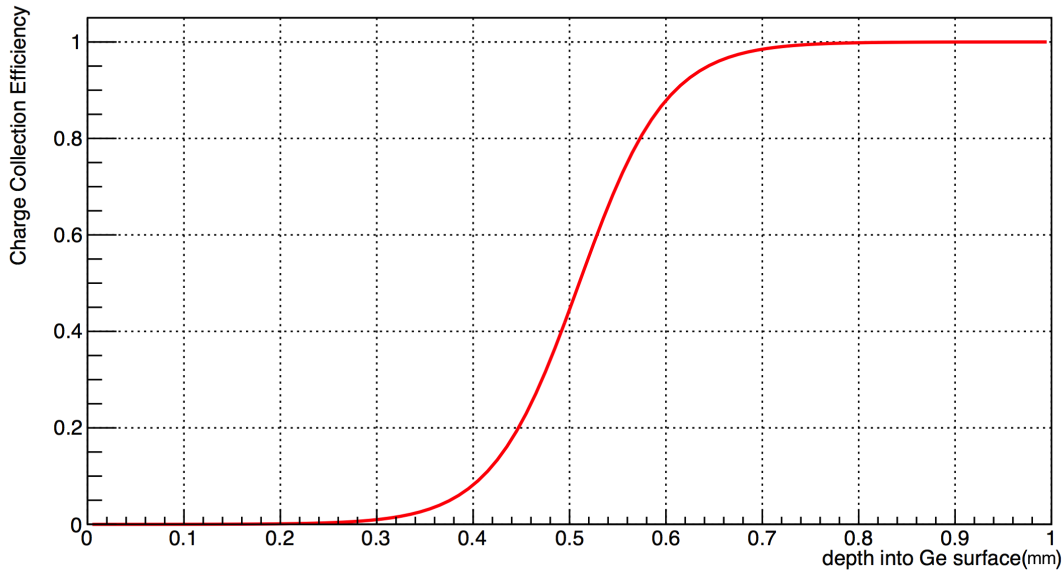


Figure 3.16: Charge collection efficiency $\varepsilon(x) = 0.5 - \tanh(11(0.51 - x))$. This function approach 0(smaller than 0.0005) when the depth x reach 0.16 mm, and approach 1 (greater than 0.9995) when the depth reach 0.86 mm.

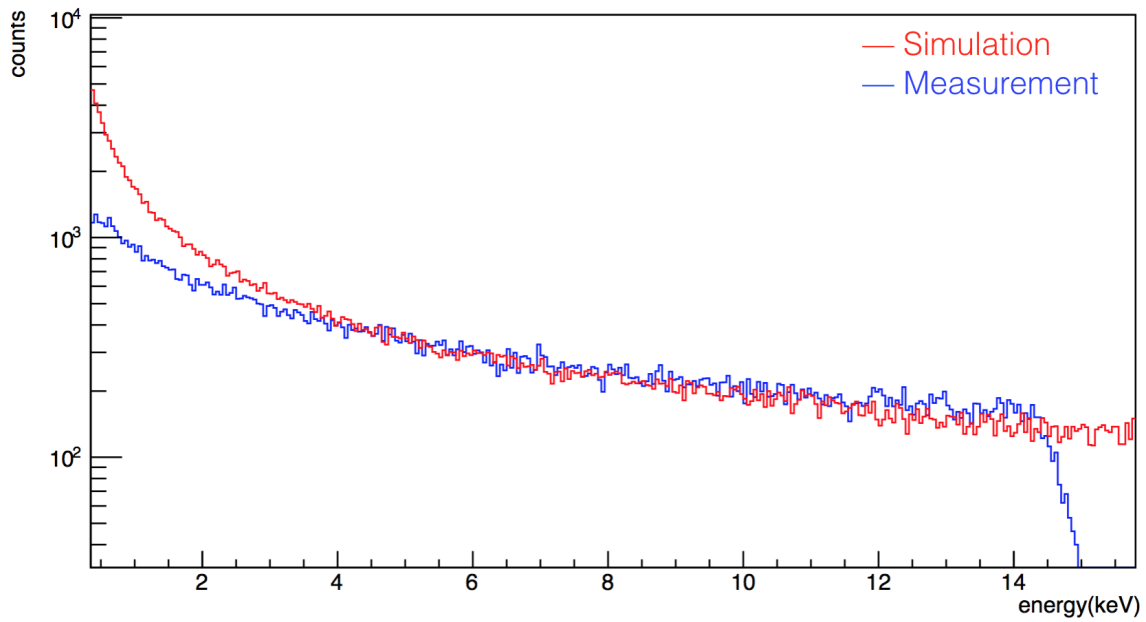


Figure 3.17: Hyperbolic tangent charge collection efficiency applies to Am-241 low energy surface spectrum from simulation, measurement and simulation data start to separate below 5 keV. The standard deviation of two spectra from 2.5 keV to 13.5 keV is 38.98.

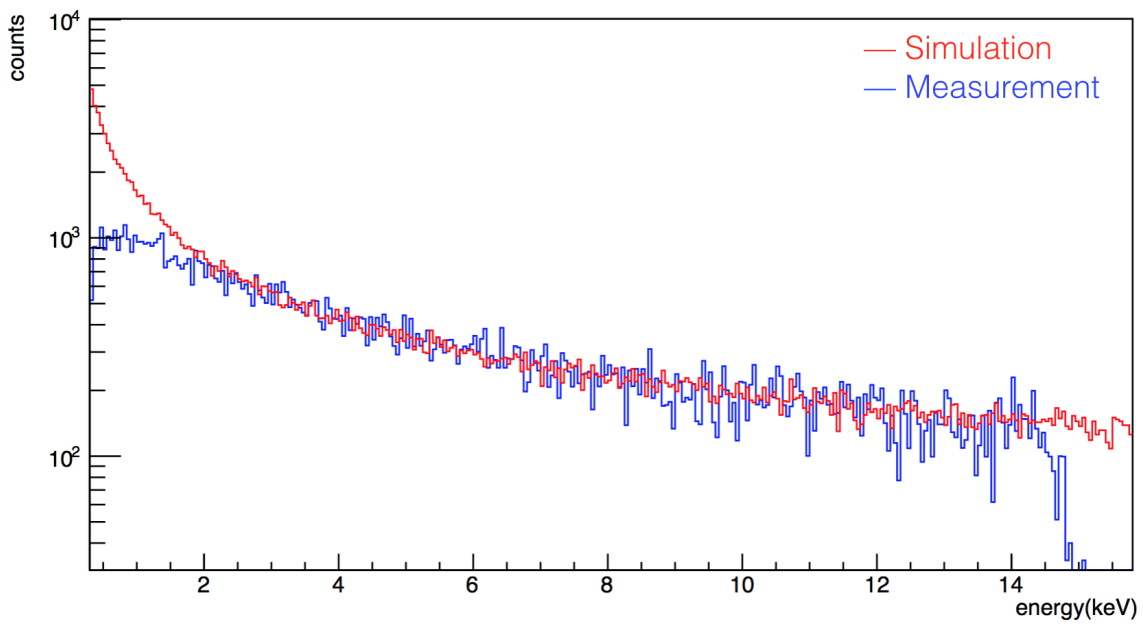


Figure 3.18: Hyperbolic tangent charge collection efficiency applies to Cs-137 low energy surface spectrum from simulation, measurement and simulation data start to separate below 2.5 keV. The standard deviation of two spectra from 2.5 keV to 13.5 keV is 47.23.

Since the p-PCGe detector will distort the energy spectrum in the surface, especially in the low-energy region, finding a suitable function for charge collection efficiency in the surface is important for understanding the p-PCGe detector. We try to conjecture the charge collection efficiency by using T-function and hyperbolic tangent.

There's a little problem in T-function profile. The parameters found from Am-241 source do not fit quite well to Cs-137, the Cs-137 simulation and measurement surface spectra are deviate a little bit. We can get another T-function with new parameters suitable for Cs-137, and compare to the parameters acquired from fitting the Am-241 source, but it is a time-consuming work. The gamma energy of Cs-137 is 661.7 keV, which is much higher than Am-241, so the events of energy deposit in the surface layer are rare for Cs-137. Therefore, it takes much time to collect the data for Cs-137 surface spectrum, and also time-consuming for finding hundreds of combinations of T-function.

For hyperbolic tangent, the problem is that the surface and dead layer depth obtained from T-function are not suitable for the hyperbolic tangent. Measurement and simulation spectra will deviate in low energy region(lower than 4 keV), it is probably due to the growing rate of the hyperbolic tangent is too slow in shallow transition layer. In fact, We have tried several different parameters for hyperbolic tangent, the deviation in low energy region is a common problem.

In summary, we believe that the T-function is a function closer to the real charge collection efficiency, but it needs some adjustment.



Chapter 4

Data Analysis

4.1 Parameterization

Every signal send out by the detector will be stored in a waveform, we need to parameterize these waveforms for off-line analysis. Figure 4.1 is a typical waveform for a physic event.

Some parameters we need to parameterize from original pulse, the most important parameters and selection rules are listed below:

1. Maximum point and the corresponding time bin of the pulse is searched from 10-60 μs window.
2. Minimum point and the corresponding time bin of the pulse is searched from 0-96 μs window.
3. Amplitude is the height of the maximum point after subtracting the pedestal.
4. Pedestal is calculated by averaging the amplitude of every event from 0 to 10

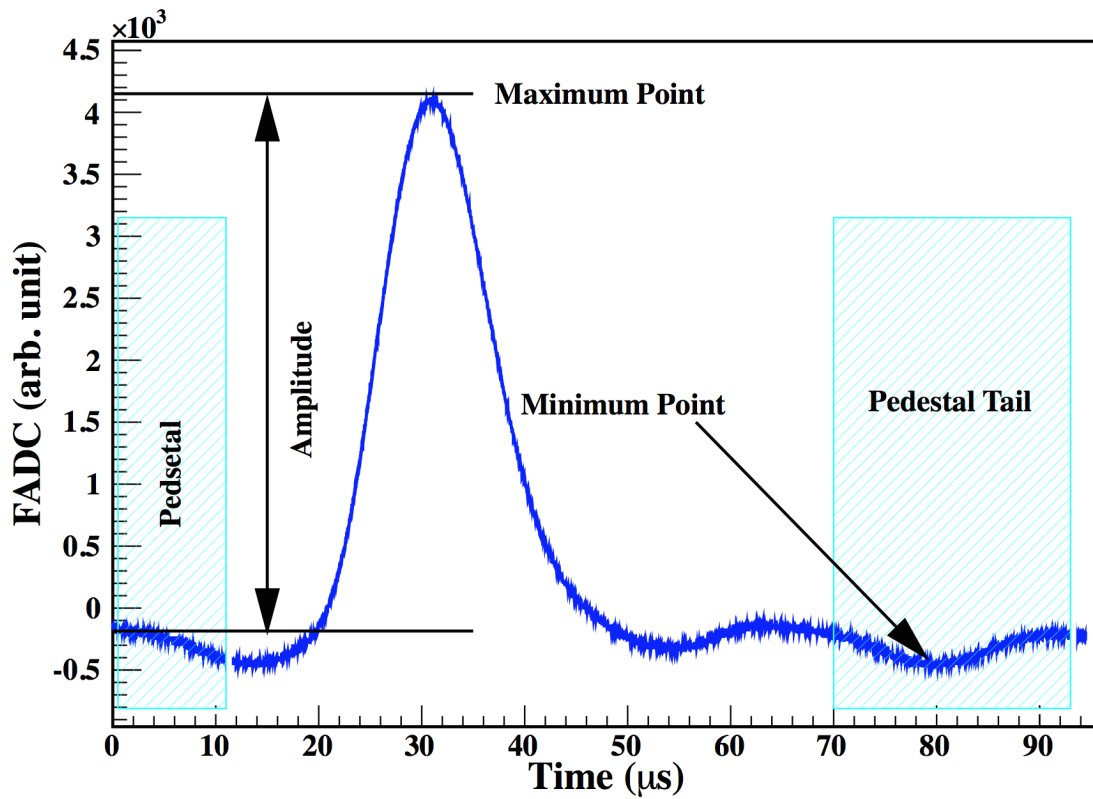


Figure 4.1: A typical waveform with some relevant parameters.

μs , and pedestal tail is calculated by averaging the amplitude of every event from 70 to 96 μs :

$$ped = \frac{1}{10\mu s} \sum_{t=0}^{10\mu s} V(t), \quad pedtail = \frac{1}{26\mu s} \sum_{t=0}^{26\mu s} V(t)$$

All the information for off-line analysis will be stored in a ROOT ntuple file.



4.2 Event Selection

For the signals we received, not all of them are the events we needed, by using some selection rules during off-line data analysis to pick up the needed events and eliminate the unwanted events like noise and background events. This section will present how the selections have proceeded.

4.2.1 Basic Cuts

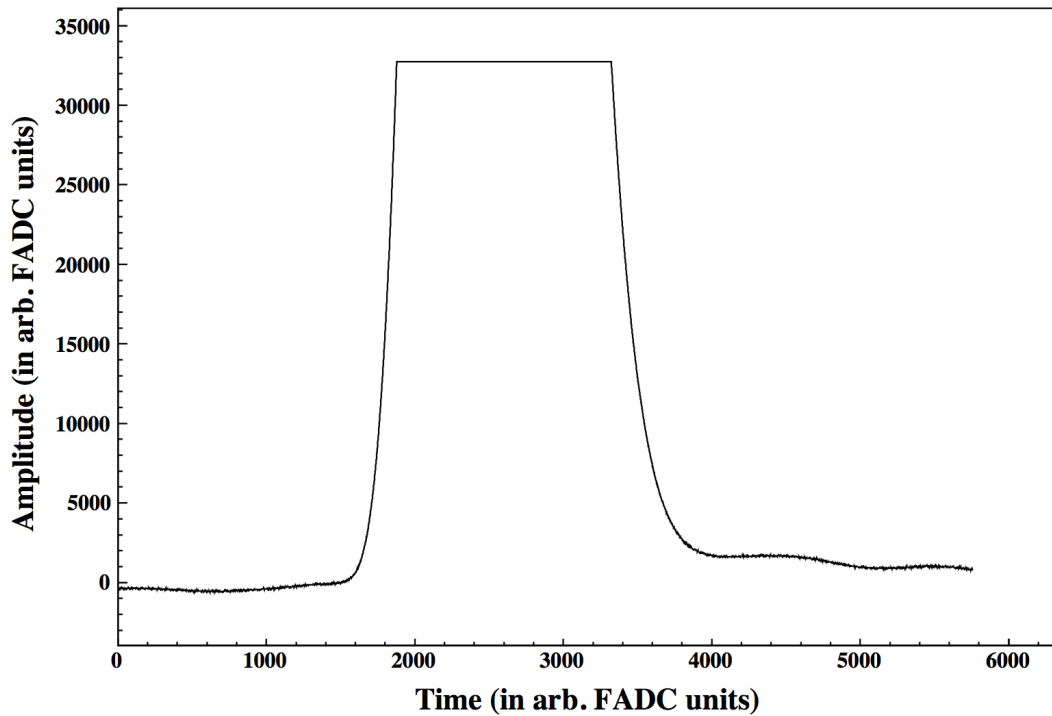


Figure 4.2: A saturated event which will be eliminated because the energy information is missing.

The main purpose of basic cut is to eliminate the noise events, the waveform

parameters of a normal physic events will satisfy some conditions. The spirit of basic cut is to get rid of the events which do not meet these conditions.

The shaping amplifier will shape and amplify the signals of the preamplifier. The amplification factor will cause high energy events to be saturated. We will eliminate this kind of event because the information of energy deposit in the detector is missing. A saturated event is shown in Figure 4.2.

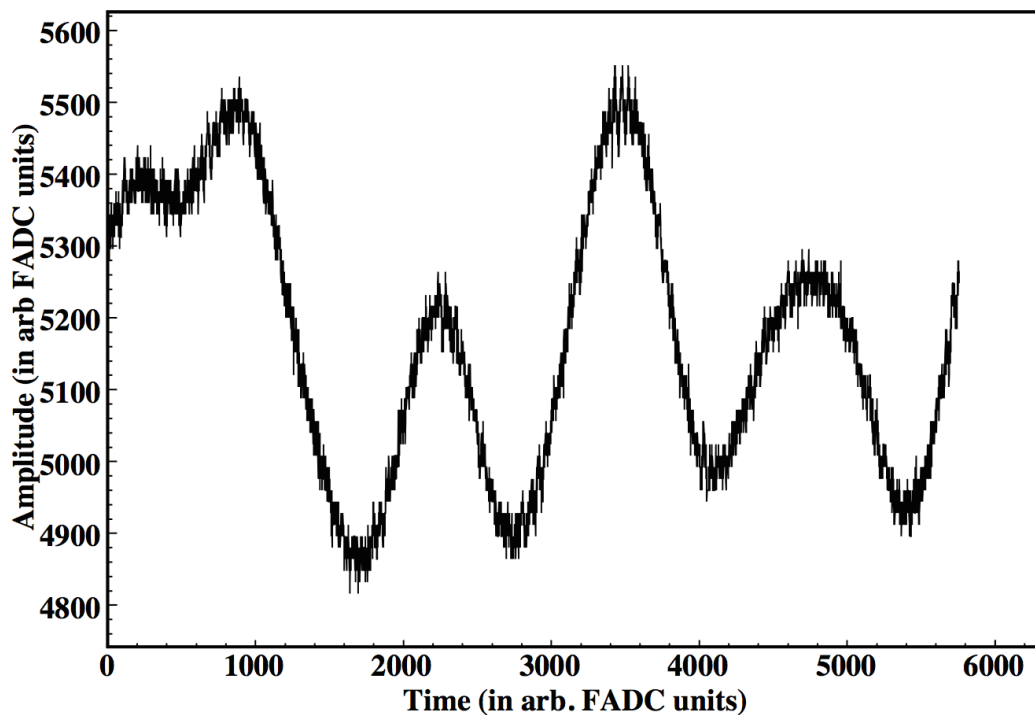


Figure 4.3: A multi-peaked noise event.

Unlike a normal physic event which only have a single peak, the waveform of noise events (Figure 4.3) has multi-peaks. We can depict a plot with pulse pedestal versus amplitude, the events distribution in this plot should be in a given area. We

will discard any of the events do not locate in this specific area. The pulse pedestal versus amplitude plot is depicted in Figure 4.4, events located outside the lines will be discarded.

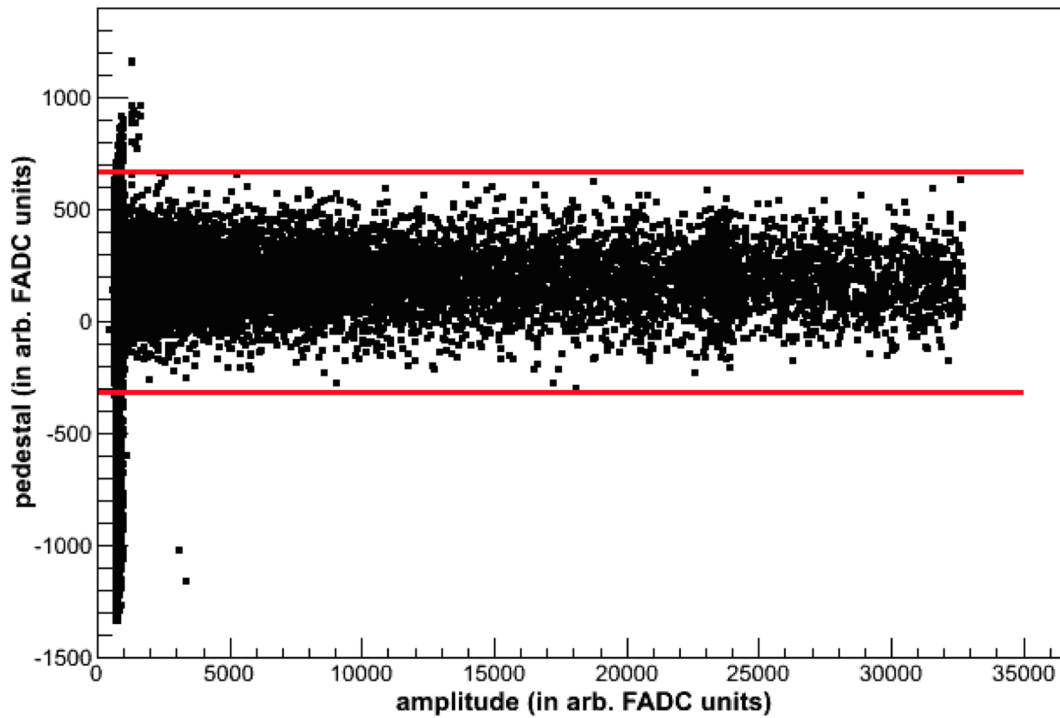


Figure 4.4: The relation between pedestal and amplitude, only events located in red lines will be considered in further analysis.

For Germanium detector, the relation between charge (area under the pulse with maximum height) and amplitude (difference of peak height and pedestal height) of a physic event should be linear. Therefore, we may further discard unwanted events by depicting a charge versus amplitude plot. This plot is shown in Figure 4.5, any events outside the red lines will be discarded.

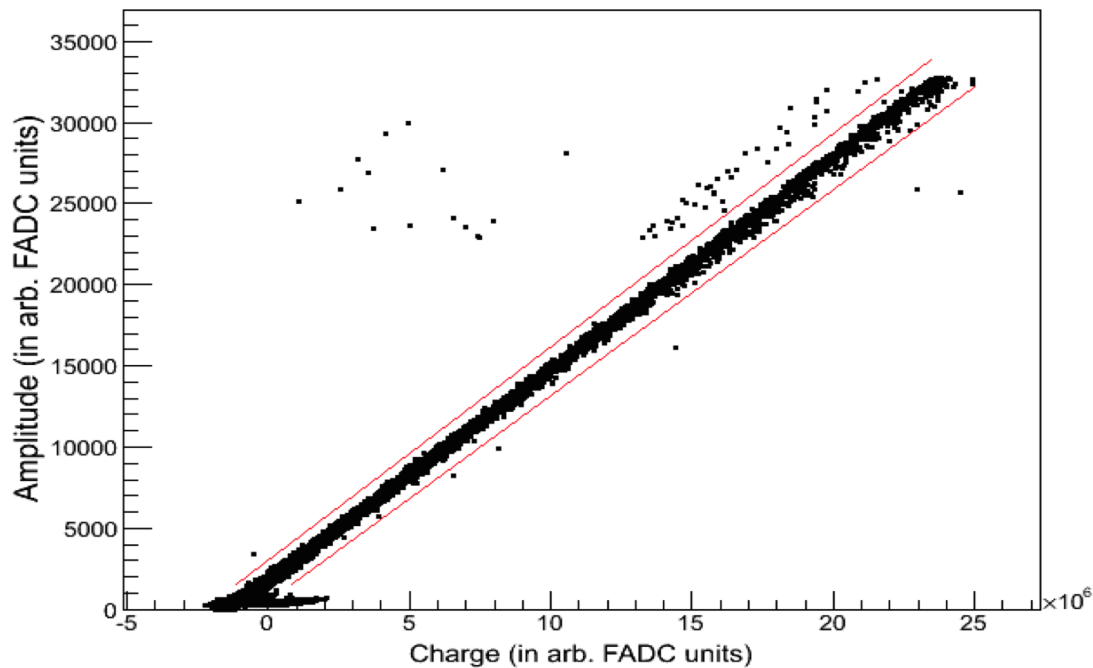


Figure 4.5: Relation between charge and amplitude, only events located in red lines will be considered in further analysis.

The above procedures are the basic cuts which are the most fundamental cuts we apply to every data sets. We sometimes apply few more cuts to the data, depending on the data taking condition or some specific purposes.

4.2.2 Cosmic Ray Veto

The cosmic ray veto detector is built by 16 pieces of plastic scintillators; it allows us to reject cosmic ray muons and cosmic ray muon induced events. Thus we can suppress the background. As mentioned in chapter 2, we record the time difference between Ge trigger and the last hit in the plastic scintillators. By depicting a 2-

dimensional distribution of the time difference versus energy deposit in Ge crystal in Figure 4.6, we can notice many events are concentrating in a single band which we call veto band. Germanium signals are processed by shaping amplifier with 6 μs shaping time, and a constant threshold discriminator helps in defining rise time, low energy events have a longer rise time causes further delay in the arrival of Germanium signals, this will result in a longer time difference for low energy events. It is why the veto band is bending up in low energy region.

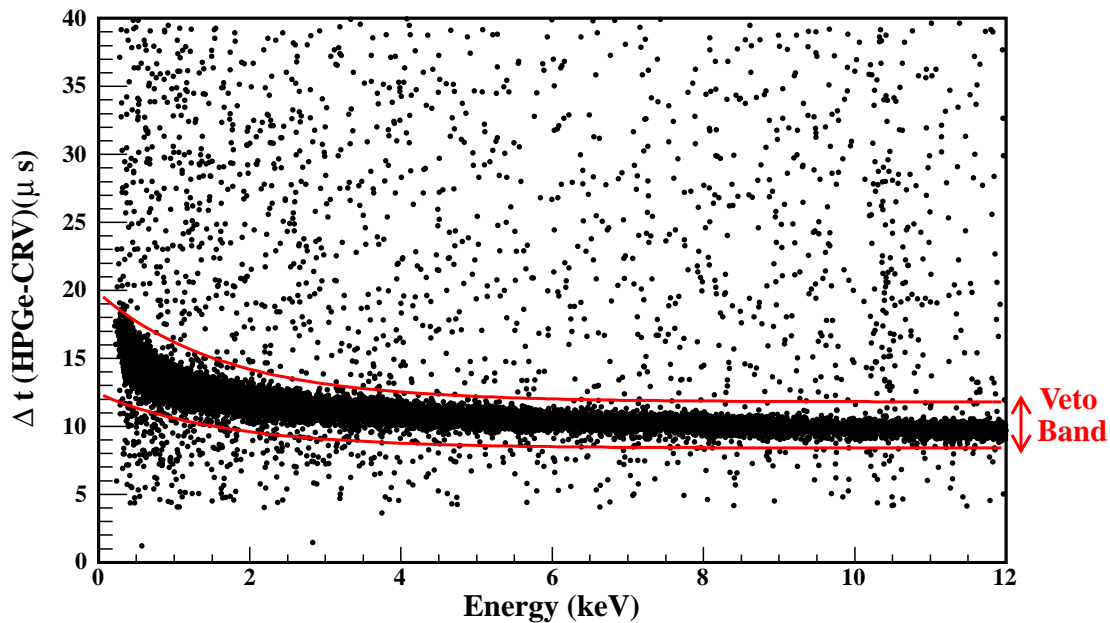


Figure 4.6: A 2-dimensional distributional of the time difference between Ge trigger and the last hit in cosmic ray veto panels versus the energy deposited in the Ge crystal, we can clearly see a strong concentration in a single band.

The events locate in veto band have a strong correlation to the background events like cosmic ray and environmental gamma, and uncorrelated to the events

like neutrino or WIMPs-induced signatures. The events outside veto band are CRV events, and events inside veto band are CRT events. The CRV (cosmic ray veto) cut efficiency is 92% for various periods of data taking with about 25% suppression factor in energy region 4 keV to 8 keV. The suppression factor is defined by the ratio of the remaining number of events after applying the criterion to the number of events before applying the criterion. The spectra before and after applying the CRV criteria is shown in Figure 4.7.

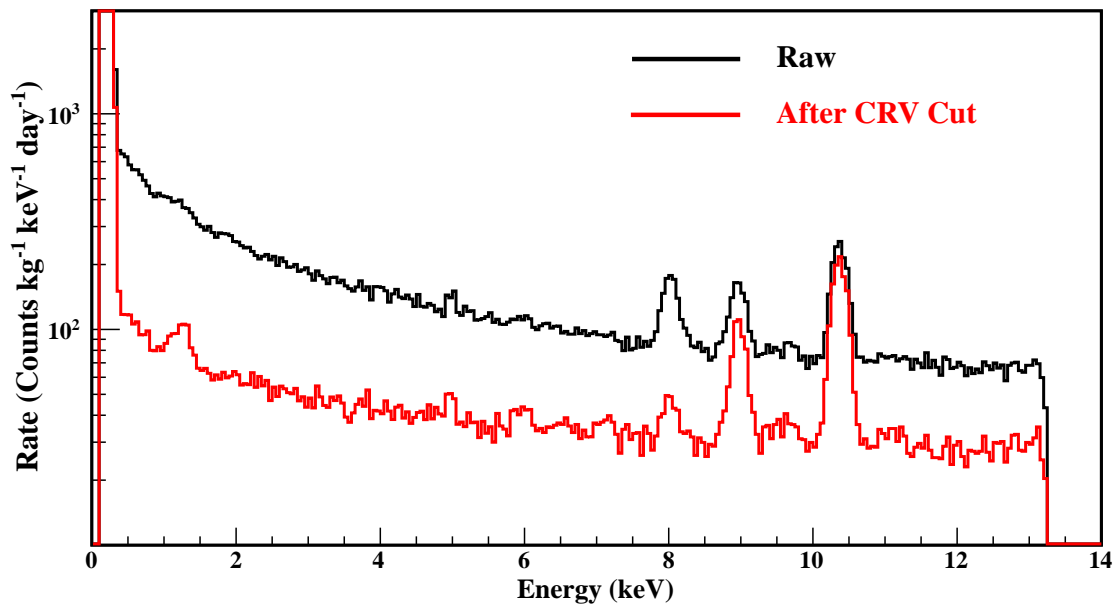


Figure 4.7: The spectra before and after applying the CRV criteria.

4.2.3 Anti-Compton Veto

The anti-Compton detector can help us further eliminate the background events (mostly gamma ray-like). The NaI(Tl) and HPGe detector configuration are shown

in Figure 2.5. For $\bar{\nu}_e$ and WIMP, the possibility of both interacts with NaI(Tl) and Ge crystal is very small. Thus we have to eliminate this kind of events by applying ACV (Anti-Compton Veto) criterion. The events inside signal band are ACV events, and events outside signal band are ACT events.

A 2-dimensional distribution of NaI(Tl) signal pulse amplitude versus energy deposit in Ge detector is depicted in Figure 4.8.

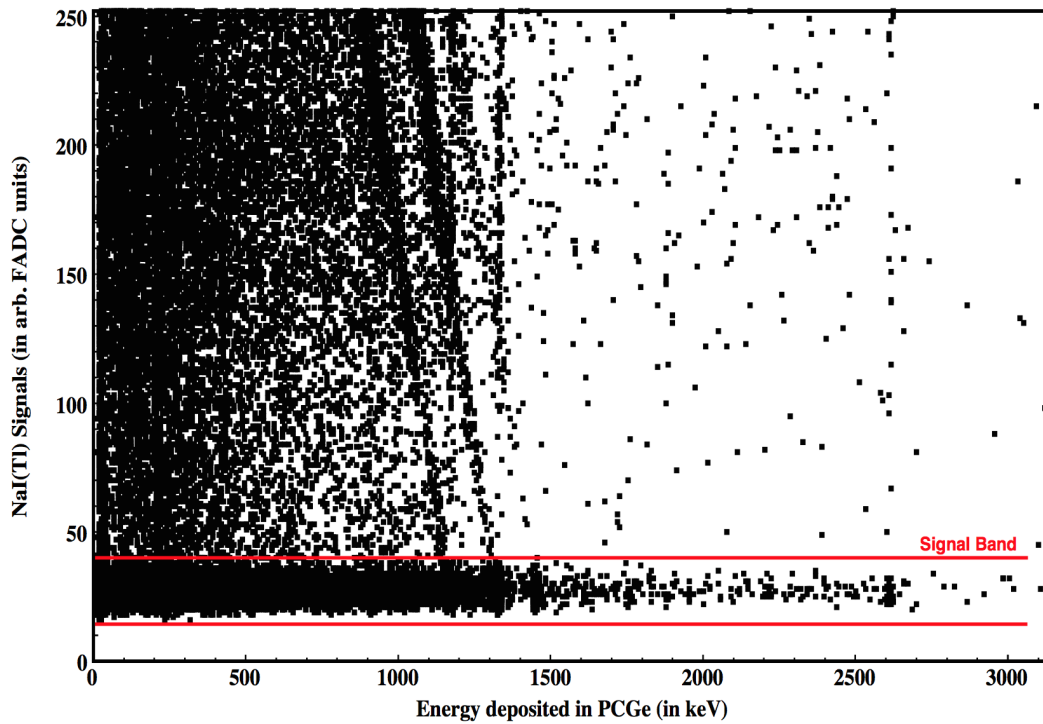


Figure 4.8: A 2-dimensional distribution of NaI(Tl) signal pulse amplitude versus energy deposit in Ge detector, events outside the signal band (red lines) should be eliminated.

We only further consider the events which do not interact with NaI(Tl) detector

(small pulse amplitude), but interact with Ge detector (they deposit energy in Ge crystal), i.e., the events in the signal band. The suppression factor of ACV criterion is 15% in energy region 4 keV to 8 keV. The spectra before and after applying the ACV criteria is shown in Figure 4.9.

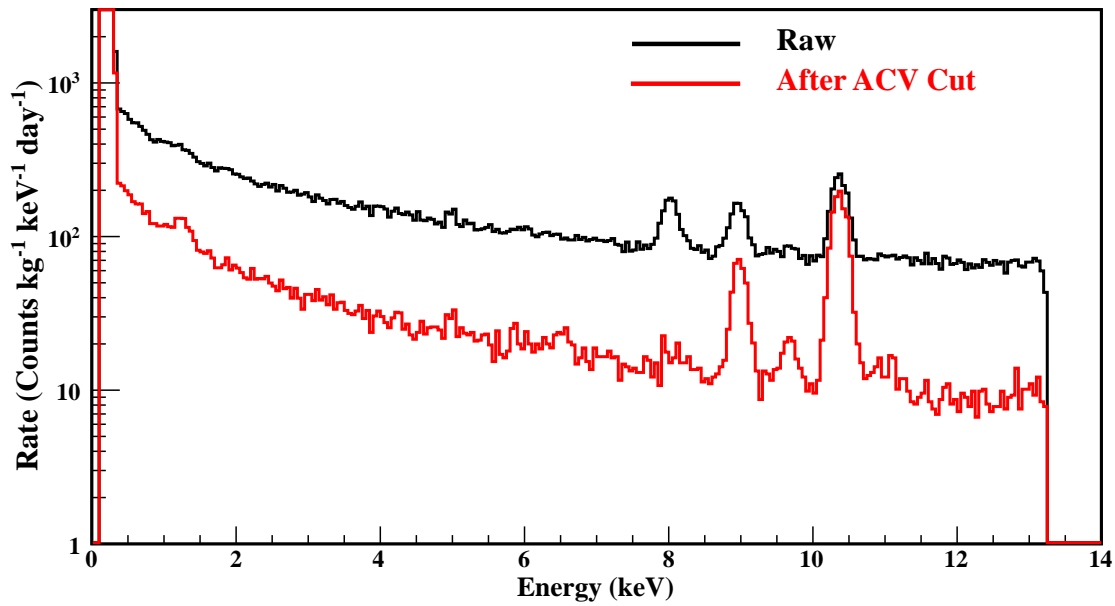


Figure 4.9: The spectra before and after applying the ACV criteria.

With ACV and CRV cut, we can perform 4 different combinations of energy spectra, by applying (1)CRV and ACV criteria (2)CRV and ACT criteria (3) CRT and ACV criteria (4)CRT and ACT criteria. Figure 4.10(a) and 4.10(b) are the CRT+ACV and CRV+ACT energy spectra respectively.

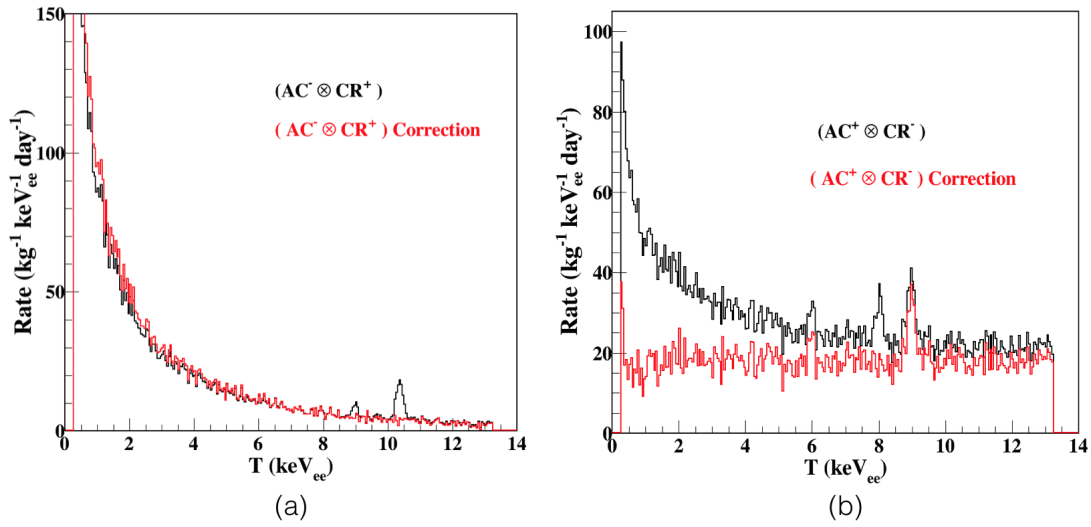


Figure 4.10: (a) A spectrum after applying CRT and ACV criteria. Most of these events are cosmic ray induced neutron events in shielding. We need to correct the spectrum because of the detection efficiency of cosmic ray veto system, and the peaks around 10 keV are from Ge crystal.

(b) A spectrum after applying CRV and ACT criteria. Most of these events are gamma events produced in shielding. We need to correct the spectrum again because of the detection efficiency of cosmic ray veto system.



Chapter 5

Internal Background

5.1 Introduction

We are looking for the extremely rare signal in our experiment, suppressing background level is crucial. It is important for us to understand what might be the sources of background and how much do they contribute to the energy spectrum. There are two main sources of our background: photons and neutrons. This chapter will discuss where are photons and neutrons coming from, and what will they affect to the spectra.

Because of neutrons, several cosmogenic isotopes are decaying via electron capture in germanium crystal, resulting some X-ray peaks below 12 keV in Ge low energy VrV (CRV+ACV cut, after correction) spectrum. A typical Ge VrV spectrum is shown in Figure 5.1. However, those X-ray peaks are not the only participant in the VrV spectrum; we also have other backgrounds contribute to the VrV spectrum.

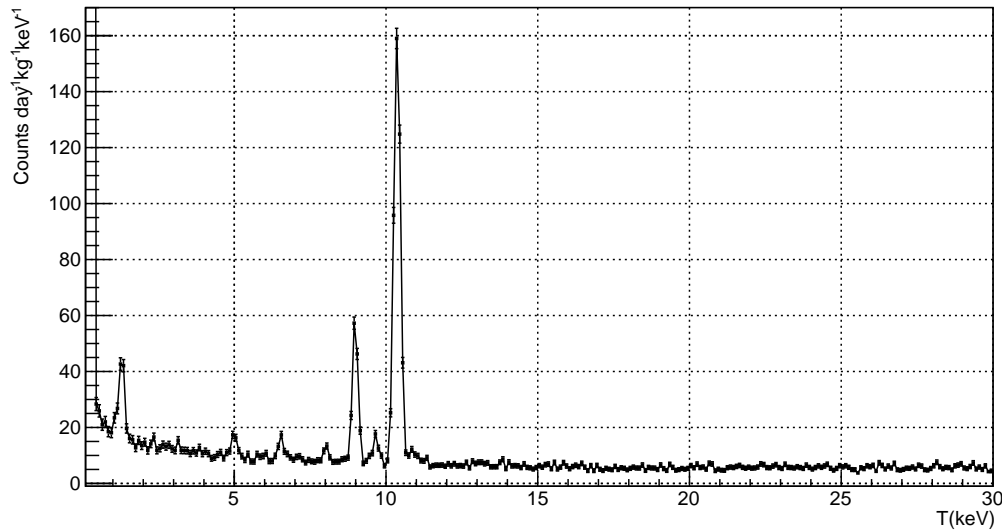


Figure 5.1: A typical Germanium detector low energy VrV (CRV+ACV cut, after correction) spectrum, including several K/L shell peaks and background.

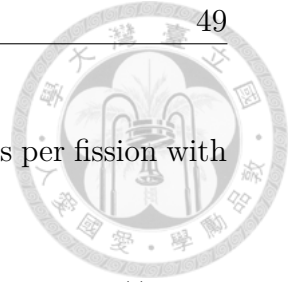
We can use the Ge low energy VrV spectrum to estimate the 3H decay rate upper limit.

5.2 Background Sources

5.2.1 Neutron Background

Local radioactivity and cosmic ray muons are the main sources of neutron background. For neutrons from local radioactivity, two of the process can be considered:

- (i) Alpha particles emit from Uranium and Thorium decay chain can interact with light elements and produce neutrons via alpha-neutron reaction.



- (ii) Spontaneous fission of ^{238}U will produce average 2.07 neutrons per fission with 4.47×10^9 years of half-life.[2]

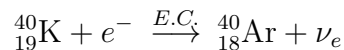
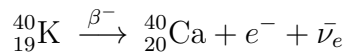
Cosmic ray muons can produce fast neutrons by the following process, (i)muon spallation, (ii)muon scattering with neutrons bound in nuclei, (iii)photo-nuclear reactions and (iv)Secondary neutrons produced in the above three processes. The high energy fast neutrons produced in these processes can easily penetrate our shielding and hit Ge crystal.[3]

5.2.2 Photon Background

In KSNL, photon background is causing by two main sources. Environmental radioactivity and cosmic ray induced photon.

The decay of Uranium-238, Thorium-232 and Potassium-40 are the main cause of environmental radioactivity. In ^{238}U decay chain, the strongest photon line are ^{234}Th , ^{214}Pb and ^{214}Bi , while ^{228}Ac , ^{212}Pb and ^{212}Bi are the strongest line in ^{232}Th decay chain. Figure 5.2 show the decay processes of ^{238}U and ^{232}Th series.

The natural abundance of ^{40}K is 0.0117%, with 89.28% possibility decay to ^{40}Ca via beta decay and 10.72% decay to ^{40}Ar via electron capture,



When ^{40}K decay to ^{40}Ar , it will also emit a 1460.82keV gamma ray which will

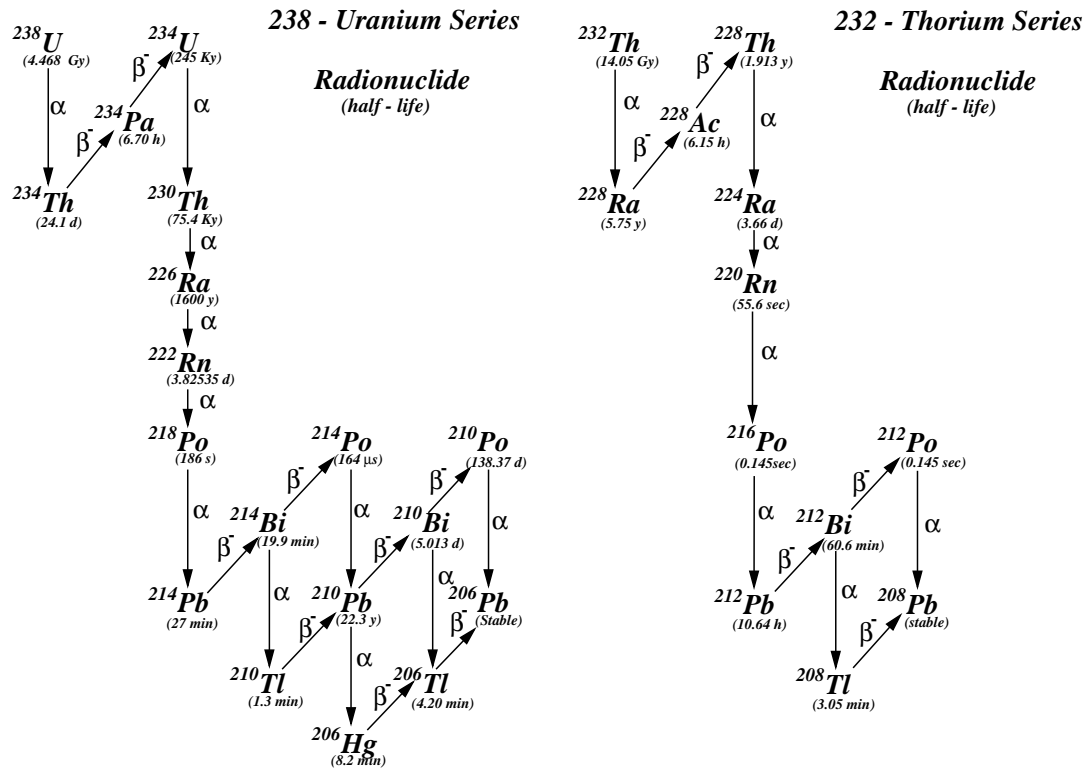


Figure 5.2: Decay chain for Uranium-238 and Thorium-232 series.

become one of our photon background.

Both neutron background and photon background are associated with the cosmic ray, most of the materials can produce radionuclides because of the cosmic ray hadronic components, and create a secondary photon background. For example, we are using copper in our detector system, but copper can create unstable nuclides when cosmic ray neutrons hit the copper. These unstable nuclides will decay to other nuclides via various decay modes like beta decay, gamma decay, and electron capture, and some of these decay will contribute to part of the photon background.

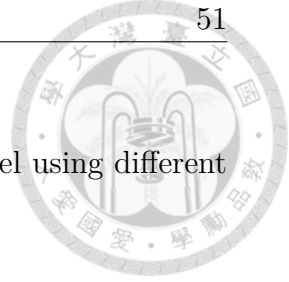


Table 5.1: The production rates of Cosmogenic nuclides at sea level using different cosmic neutron spectra.

	Neutron spectra from Ziegler	Neutron spectra from Gordon et al.
^{56}Co	$22.9 \text{ kg}^{-1}\text{day}^{-1}$	$20.0 \text{ kg}^{-1}\text{day}^{-1}$
^{57}Co	$88.3 \text{ kg}^{-1}\text{day}^{-1}$	$74.1 \text{ kg}^{-1}\text{day}^{-1}$
^{58}Co	$159.6 \text{ kg}^{-1}\text{day}^{-1}$	$123.0 \text{ kg}^{-1}\text{day}^{-1}$
^{60}Co	$97.4 \text{ kg}^{-1}\text{day}^{-1}$	$55.4 \text{ kg}^{-1}\text{day}^{-1}$
^{54}Mn	$32.5 \text{ kg}^{-1}\text{day}^{-1}$	$27.7 \text{ kg}^{-1}\text{day}^{-1}$
^{59}Fe	$6.5 \text{ kg}^{-1}\text{day}^{-1}$	$4.9 \text{ kg}^{-1}\text{day}^{-1}$
^{46}Sc	$3.8 \text{ kg}^{-1}\text{day}^{-1}$	$2.7 \text{ kg}^{-1}\text{day}^{-1}$

The cosmogenic nuclides produced in natural copper and its production rate at sea level are shown in Table 5.1[4]. The production rate is expressed in $\text{kg}^{-1}\text{day}^{-1}$, and the numbers are obtained by two different cosmic neutron spectra.

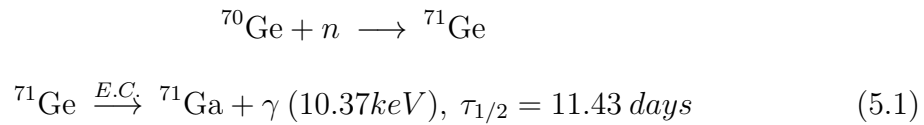
5.3 X-ray peaks

In the last section, we know that cosmic ray hadronic components will interact with copper and create photon background; likewise, cosmic ray neutron will also interact with germanium crystal and create the internal background. First, cosmic ray neutron will hit germanium nucleus and become an unstable germanium isotope, and then decay to another nuclide via electron capture(E.C.) and emit an X-ray. Table 5.2 show the X-ray lines observed in the n-PCGe low energy VrV spectrum due to the exposure of cosmic ray neutron. The creation process of the most dominated

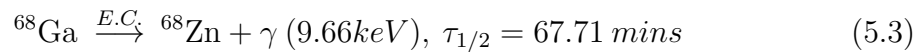
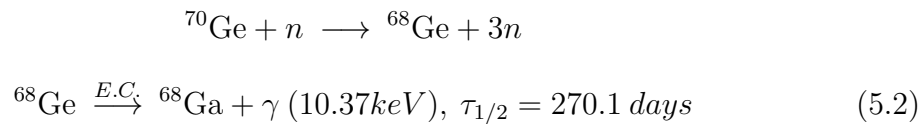


X-ray peaks in spectrum is listed below:

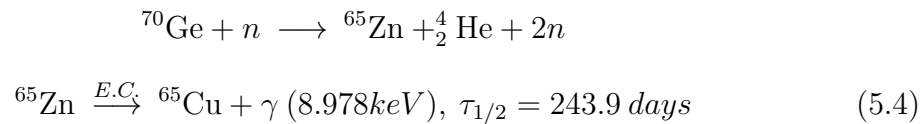
For thermal neutron case:



For fast neutron case:



It can be noted that 9.66 keV peak is decay from part of the 10.37 keV peak, these two peaks have a dependency.



As we can see, L-shell energy are very close to each other, and our energy resolution is not enough to distinguish these lines, resulting these multiple peaks look like a single peak around 1.2 keV in VrV spectrum. Also, the intensity of L-shell lines and K-shell peaks are correlated, so for the small K-shell peaks like ${}^{55}\text{Fe}$ and ${}^{49}\text{V}$, their L-shell peaks are hard to observe.

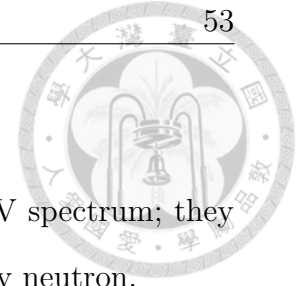


Table 5.2: These radionuclides are observed in the low energy VrV spectrum; they were produced in Ge crystal because of exposure to the cosmic ray neutron.

Parent Nuclide	Daughter Nuclide	Daughter K-shell Energy (keV)	Daughter L-shell Energy (keV)	Parent Half-life
$^{73,74}\text{As}$	Ge	11.103	1.142	80.30 day, 17.77 day
$^{68,71}\text{Ge}$	Ga	10.367	1.298	270.95 day, 11.43 day
^{68}Ga	Zn	9.659	1.197	67.71 min
^{65}Zn	Cu	8.979	1.096	243.66 day
^{55}Fe	Mn	6.539	0.769	2.737 year
^{49}V	Ti	4.966	0.564	329 day

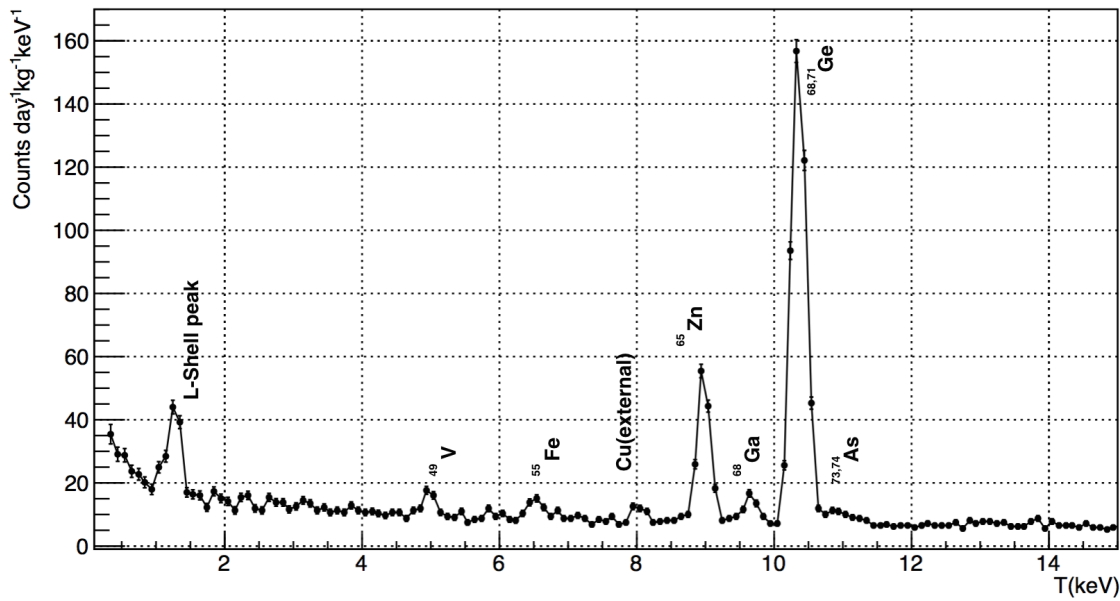


Figure 5.3: The location of X-ray lines in low energy VrV spectrum from a 500g n-PCGe detector.

In Figure 5.3, we can see a peak locate at 8.031keV which did not mention in Table 5.2 because this radionuclide is not generated inside the Ge crystal, this X-ray line comes from the cylindrical OFHC copper cover surrounding Ge crystal.

5.4 Tritium Upper Limit

Because of expose to the cosmic ray neutron, tritium will be produced from various Ge isotopes in Germanium crystal, the production cross section of 3H is depended on different Ge isotopes and neutron kinetic energy, their relationship are shown in Figure 5.4.[5] generated by TALYS code 1.0.[6]

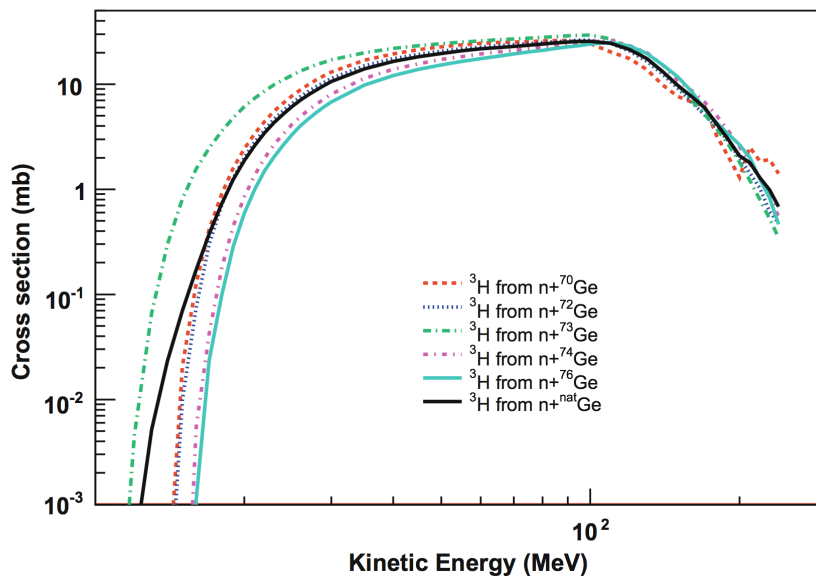


Figure 5.4: 3H production cross section vary from different Ge isotopes and neutron kinetic energy.[5]

After tritium was produced in Ge crystal, it will then 100% decay to 3He via beta

decay with a 12.32 years half-life, an electron will be released during this process and will soon be absorbed by Ge crystal, then become one of the important background in our experiment, the ${}^3\text{H}$ decay process:

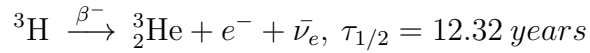


Figure 5.5 show the tritium decay spectrum is a continuous spectrum with an end point around 18.6 keV depends on the mass of electron antineutrino[7]. We can roughly estimate the Tritium decay rate by only using a flat photon background, Gaussian peaks, and ${}^3\text{H}$ beta decay spectrum to reproduce the low energy VrV spectrum.

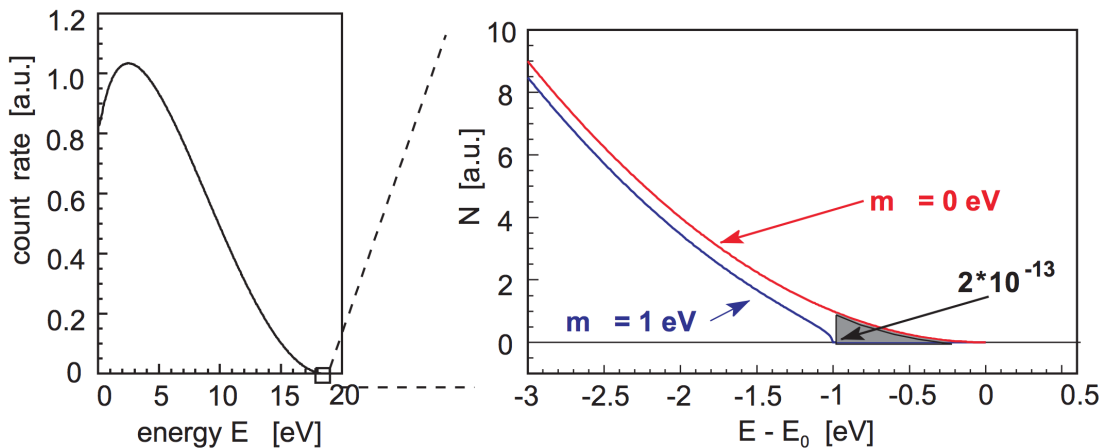
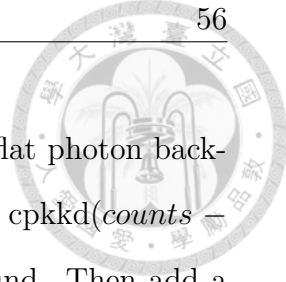


Figure 5.5: ${}^3\text{H}$ beta decay spectrum and the end point around 18.6 keV depend on the mass of electron antineutrino. Plot on the right side is the end point zoom, blue line and red line means the electron antineutrino mass = $1 \text{ eV}/c^2$ and mass = $0 \text{ eV}/c^2$ respectively.[7]



In Figure 5.1, the energy region from 20 keV to 30 keV is the flat photon background, by fitting a constant number in this region, we get 5.68 cpkcd ($counts - kg^{-1} keV^{-1} day^{-1}$) to be our initial value of flat photon background. Then add a 3H decay spectrum with adjustable intensity to fit the experiment data. The data fitting is performed from 4 to 18 keV. Depending on the height of 3H decay spectrum, we can get a number for Tritium decay rate. The result is shown in Figure 5.6. Also, for the production rate, it depends on the history of Ge crystal. The 500g n-PCGe detector is manufactured in France, and there is no evidence for that we can remove the Tritium when growing Ge crystal. Tritium was already existed in Ge crystal when it was manufactured. After we moved 500 n-PCGe detector to KSNL, the production rate of Tritium will decrease due to the lower cosmic ray neutron flux. But the Tritium decay half-life is 12.32 years, we need several years to let production and decay re-enter an equilibrium state. So we conjecture that the Tritium production rate is close to the decay rate, say 32.5 atoms/kg-day.

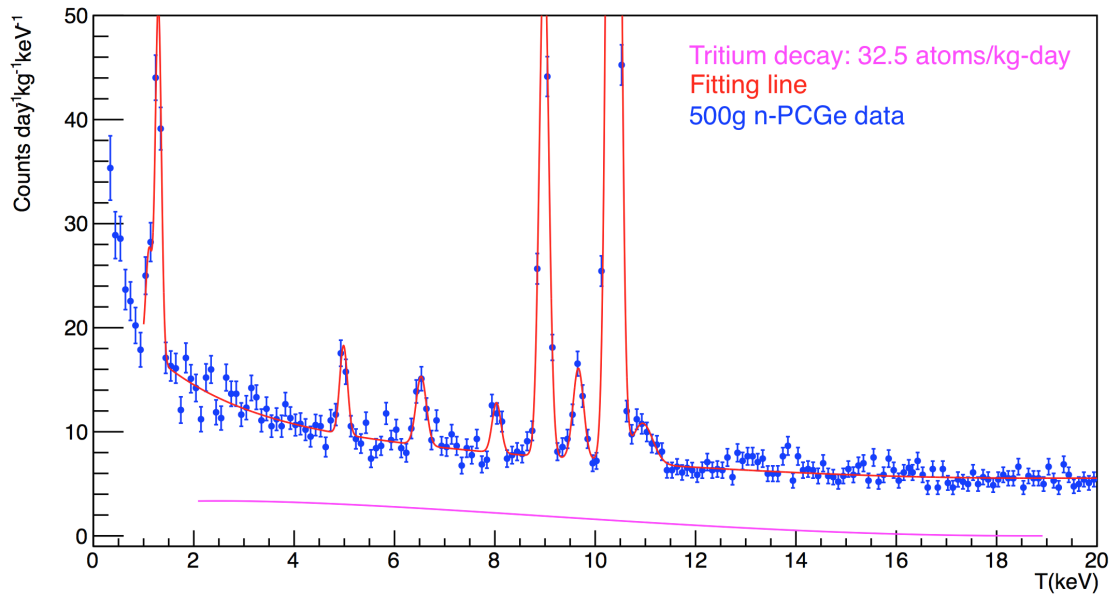
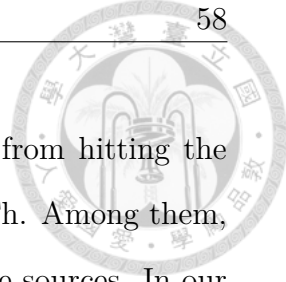


Figure 5.6: The result of the ${}^3\text{H}$ decay rate estimation. Magenta line is the ${}^3\text{H}$ decay spectrum, and the red line is a fitting line formed by ${}^3\text{H}$ decay spectrum + flat photon background + Gaussian peaks. The ${}^3\text{H}$ decay spectrum indicates the decay rate upper limit is $32.5 \text{ kg}^{-1} \text{ day}^{-1}$.

5.5 Summary

In this chapter, we introduce the internal background of Ge detector and estimate the upper limit of tritium decay rate. The estimation of Tritium beta decay rate can be improved. We try to reproduce the 500g n-PCGe detector low energy VrV spectrum by using only three ingredients, including a flat photon background, gaussian x-ray lines, and tritium beta decay spectrum. According to a talk by CoGeNT[8], there are various sources of backgrounds contribute to their energy spectrum, including



resistor gamma backgrounds (U/Th/K), muon-induced neutrons from hitting the shielding, tritium beta decay, and cavern (α,n) neutrons from U/Th. Among them, resistor gamma and muon-induced neutrons are the most dominate sources. In our experiment, the resistor gamma backgrounds can be vetoed by the anti-Compton detector during offline analysis, and muon-induced neutron events are our CRT+ACV spectrum. However, the cavern (α,n) neutrons from U/Th inside shielding is a possible source to contribute in Ge low energy VrV spectrum. We can try to investigate how many neutrons are produced inside the shielding by installing a neutron detector, then re-calculate the tritium beta decay rate.

In summary, to increase the accuracy of tritium decay rate upper limit, we need to investigate that are there any other sources can contribute to Ge internal background.



Chapter 6

Summary

1. The thick lithium outer contact of p-PCGe will cause the surface effect, resulting that we cannot fully collect the energy deposit in the surface region, the charge collection efficiency is a function of depth. We have two models for this function, to find the parameters in the models, try to apply the models on simulation data of Am-241 then compare to experimental data. Among these two models, we believe that the T-function profile is closer to the real charge collection efficiency, while the hyperbolic tangent will transfer too many events into energy region below around 4 keV. We can further use the Cs-137 source to find the new parameters in T-function, and compare the two sets of parameters acquired by Cs-137 and Am-241 sources. Perhaps there are some adjustments we can do in the T-function.

2. To search for a rare and low energy event, it is important for us to understanding the background composition. We have both passive shielding and active shielding to veto most of the ambient background, but Ge will show activities due to the expo-

sure to cosmic ray neutron. The x-ray lines in Ge low energy spectrum (CRV+ACV cut) are easier to understand because the gamma emits from electron capture is monoenergetic. However, the Tritium in Ge crystal will decay to Helium via beta decay with a half-life of 12.32 years; this decay is a continuous spectrum with an end-point around 18.6 keV. By adding flat photon background and Tritium beta decay spectrum, then fit the data acquired by 500g n-PCGe detector from 4 to 18 keV, We try to estimate the contribution caused by Tritium in Ge internal background. The Tritium decay rate upper limit in Ge crystal is around 32.5 atoms/kg-day with 95% confidence level. To increase the accuracy, we can investigate other candidates for contributing to the background, for example, neutrons inside the shielding as mentioned in the last chapter.



Bibliography

- [1] Henry T. Wong. Ultra-low-energy germanium detector for neutrino-nucleus coherent scattering and dark matter searches. *Modern Physics Letters A*, 23:1431–1442, 2008.
- [2] John Shultis and Richard Faw. *Fundamentals of Nuclear Science and Engineering*, page 141. CRC Press, 2007.
- [3] Y-F. Wang et al. Predicting neutron production from cosmic-ray muons. *Phys.Rev. D*, 64, 2001.
- [4] S. Cebrián et al. Cosmogenic activation in germanium and copper for rare event searches. *Astroparticle Physics*, 33:316–329, 2010.
- [5] D.-M. Mei, Z.-B. Yin, and S. R. Elliott. Cosmogenic production as a background in searching for rare physics processes. *Astroparticle Physics*, 31:417–420, 2009.
- [6] A. Koning, S. Hilaire, and M. Duijvestijn. Talys code, <http://www.talys.eu/>.
- [7] L. Bornschein for the KATRIN-Collaboration. The katrin experiment - a direct



measurement of the electron antineutrino mass in the sub-eV region. *Nuclear Physics A*, 752:14c–23c, 2005.

- [8] John L. Orrell. Cogent dark matter experiment. Technical report, Pacific Northwest National Laboratory, 2013.